Tissue clearing and its applications in neuroscience

Hiroki R. Ueda [1,2] *, Ali Ertürk* [3,4,5], *Kwanghun Chung* [6,7,8,9,10,11,12], *Viviana Gradinaru* [13], *Alain Chédotal* [14], *Pavel Tomancak* [15,16] *and Philipp J. Keller* [17]

Abstract | State-of-the-art tissue-clearing methods provide subcellular-level optical access to intact tissues from individual organs and even to some entire mammals. When combined with light-sheet microscopy and automated approaches to image analysis, existing tissue-clearing methods can speed up and may reduce the cost of conventional histology by several orders of magnitude. In addition, tissue-clearing chemistry allows whole-organ antibody labelling, which can be applied even to thick human tissues. By combining the most powerful labelling, clearing, imaging and data-analysis tools, scientists are extracting structural and functional cellular and subcellular information on complex mammalian bodies and large human specimens at an accelerated pace. The rapid generation of terabyte-scale imaging data furthermore creates a high demand for efficient computational approaches that tackle challenges in large-scale data analysis and management. In this Review, we discuss how tissue-clearing methods could provide an unbiased, system-level view of mammalian bodies and human specimens and discuss future opportunities for the use of these methods in human neuroscience.

Tissue clearing
A method to make a biological specimen transparent by minimization of light scattering and light absorption by the biological specimen.

Hydrophobic tissue clearing
One of three major tissue-clearing methods; it uses hydrophobic (water-immiscible) reagents. It is also referred to as 'solvent tissue clearing'.

Hydrophilic tissue clearing
One of three major tissue-clearing methods; it uses hydrophilic (water-miscible) reagents. It is also referred to as 'aqueous tissue clearing' but does not always involve the use of water.

Refractive index
(RI). The ratio of the speed of light in a vacuum to its speed in a specified medium. The RI of a vacuum is 1 by definition, whereas the RI of water is ~1.33.

*e-mail: uedah-tky@umin.ac.jp

Histological techniques have been the standard procedure for investigating tissues for several decades; however, a complete understanding of biological mechanisms in health and disease requires an unbiased exploration of the whole organism, not just selected parts of tissue. This need is particularly evident in the context of the nervous system, which can be found throughout the body. Tissue-clearing methods now allow 3D imaging of intact tissues and even some entire organisms. Indeed, a century-old approach at rendering tissues transparent[1] has been almost reinvented with recent developments in tissue-clearing reagents (TABLE 1) and protocols (Supplementary Table 1), efficient fluorescent labelling and rapid volumetric imaging by light-sheet microscopy[2–14].

Three major tissue-clearing approaches are currently available: hydrophobic, hydrophilic and hydrogel-based methods[15,16] (FIG. 1); hydrophobic tissue-clearing and hydrophilic tissue-clearing methods are also referred as 'solvent' and 'aqueous' tissue-clearing methods, respectively. In general, these tissue-clearing methods, especially in highly efficient protocols, remove lipids (delipidation), pigments (decolourization) and calcium phosphate (decalcification) and aim to match the refractive indices (refractive index (RI) matching) of the specimens and the imaging media by reaching an almost complete level of transparency for intact organs and even entire adult rodent bodies. Although hydrophobic methods usually shrink the tissues and thereby allow the imaging of larger samples, hydrophilic and hydrogel-based methods, if the

reagents have low osmolarity, can expand the specimens (expansion), which further increases the transparency and effective resolution (FIG. 1).

The physical principles of these tissue-clearing methods, and how each tissue-clearing process (that is, delipidation, decolourization, decalcification, RI matching and expansion) contributes to tissue transparency, are beginning to be elucidated by considering the physical properties of organs. A recent study discovered that an organ can act as a polymer gel even in the absence of exogenous polymers[17], which was originally predicted by Tanaka and colleagues via a bottom-up approach[18,19]. If an organ acts as a polymer gel, the RI of an organ ('polymer gel') can be described by both the RI and the volume of its components ('monomers') according to a theoretical formula called the Lorentz–Lorenz relation[20,21]. Therefore, delipidation and decalcification change the RI of an organ's components and hence change the RI of the organ itself, whereas expansion can increase the volume of an organ's components, also eventually reducing the RI of the organ. In either case, these processes allow the RI of an organ to be more easily matched with the RI of the medium and this results in minimization of light scattering. In addition, the minimization of light absorption, which also contributes to transparency of the specimens, can be achieved by decolourization (removing the pigments) of an organ. Recent comprehensive chemical profiling of hydrophilic tissue-clearing reagents provides a better understanding of the chemical principles

REVIEWS

of how each chemical functional group can contribute to tissue-clearing processes[22].

In parallel to forging a better understanding of the principles underlying tissue-clearing methods, researchers are continuing to improve labelling and data-analysis tools to broaden the applications of tissue-clearing methods. Indeed, labelling options have expanded with the development of ex vivo deep-tissue labelling methods for whole mouse brain[4,23–27] and whole mouse body[6,27,28] and of in vivo systematic adeno-associated virus-based labelling of CNS and peripheral nervous system cells[29,30]. Once tissues are labelled and rendered transparent, light-sheet microscopy provides rapid 3D whole-brain imaging at subcellular resolution[31]. Some forms of light-sheet microscopy can already generate isotropic and high-resolution images with a substantially higher signal-to-noise ratio and a markedly higher resolution than for the images that can be generated by two-photon microscopy[31]. Furthermore, the development of powerful machine-learning algorithms will be essential to optimize the analysis of such large data sets, especially for image segmentation. The convergence of these diverse disciplines around the tissue-clearing methods will pave the way to unbiased 3D histological assessments, which should drastically accelerate the discovery of novel developmental, physiological and pathological mechanisms impacting whole organisms.

In this Review, we cover the landscape of rapidly emerging tissue-clearing methods and their related technologies — including labelling, light-sheet microscopy and data analysis and management — as well as applications of tissue clearing in neuroscience, especially in human studies. We then discuss the challenges and opportunities relating to the integration of these technologies to generate unbiased insights into human physiology and pathology.

Author addresses

[1]Department of Systems Pharmacology, University of Tokyo, Tokyo, Japan.

[2]Laboratory for Synthetic Biology, RIKEN BDR, Suita, Japan.

[3]Institute for Stroke and Dementia Research, Klinikum der Universität München, Ludwig–Maximilian University of Munich, Munich, Germany.

[4]Institute of Tissue Engineering and Regenerative Medicine, Helmholtz Zentrum München, Neuherberg, Germany.

[5]Munich Cluster for Systems Neurology (SyNergy), Munich, Germany.

[6]Institute for Medical Engineering and Science, Massachusetts Institute of Technology, Cambridge, MA, USA.

[7]Picower Institute for Learning and Memory, Massachusetts Institute of Technology, Cambridge, MA, USA.

[8]Department of Chemical Engineering, Massachusetts Institute of Technology, Cambridge, MA, USA.

[9]Department of Brain and Cognitive Sciences, Massachusetts Institute of Technology, Cambridge, MA, USA.

[10]Eli & Edythe Broad Institute of MIT and Harvard, Cambridge, MA, USA.

[11]Center for NanoMedicine, Institute for Basic Science, Seoul, Republic of Korea.

[12]Graduate Program of Nano Biomedical Engineering, Yonsei-IBS Institute, Yonsei University, Seoul, Republic of Korea.

[13]Division of Biology and Biological Engineering, California Institute of Technology, Pasadena, CA, USA.

[14]Institut de la Vision, Sorbonne Université, INSERM, CNRS, Paris, France.

[15]Max Planck Institute of Molecular Cell Biology and Genetics, Dresden, Germany.

[16]IT4Innovations, Technical University of Ostrava, Ostrava, Czech Republic.

[17]Janelia Research Campus, Howard Hughes Medical Institute, Ashburn, VA, USA.

Hydrophobic tissue clearing

Hydrophobic tissue-clearing approaches involve the use of organic solvents and often provide complete transparency of an intact specimen quickly[32]. For example, 3D imaging of solvent-cleared organs (3DISCO), developed by Ertürk and colleagues, can fully clear a whole adult mouse brain in 1–2 days[7,33]. Ethyl cinnamate has also been used in hydrophobic tissue clearing instead of organic solvents[11]. Because hydrophobic tissue-clearing methods are straightforward, only needing the sequential incubation of the specimen in different solutions, 3DISCO and its variants have already been widely used in imaging studies of neuronal circuits[7,33], inflammation[34], stem cells[35,36] and cancer cells[37–39], and in unsectioned rodent organs and human biopsy specimens[40]. DISCO-based methods have also been combined with deep-tissue immunolabelling approaches to study rodent embryos[4,8], human embryos[23], cancer biopsy specimens[40,41], adult mouse brains[4,26] and, more recently, whole mouse bodies (discussed later)[28].

DISCO-based methods consist of an initial dehydration step to remove water — the major light scatterer in tissues (the RI of water is 1.33, whereas the RI of soft tissues is 1.44–1.56) — and a subsequent organic solvent immersion step to extract most of the lipids and increase the RI to match the average RI of biological tissues (the RI for both organic solvents and shrunk brain tissue is ~1.56)[15]. In most of the DISCO approaches (except immunolabelling-enabled DISCO+ (iDISCO+))[34], dehydration leads to a marked shrinkage of the specimen[32]. Pan et al. developed the ultimate DISCO (uDISCO) method and shrank mouse bodies to about one third of their original size, which facilitated imaging of the entire bodies at cellular resolution by light-sheet microscopy[42]. The shrinkage of individual organs, especially CNS tissue, was isotropic; the bones also shrunk isotropically but to a lesser degree[42]. Through the use of uDISCO, the researchers visualized neuronal connectivity in the intact CNS of mice (that is, in the brain and spinal cord).

An important advantage of organic solvent-based clearing is the permanent preservation of the specimens, owing to the hardening of the cleared tissues. This allows multiple imaging sessions and long-term reanalysis of the samples, especially by immunolabelling methods, which can permanently stabilize the endogenous fluorescent signal[28]. Although clearing and imaging increasingly larger samples are valuable steps in the unbiased analysis of tissues, thorough labelling of large tissues with specific dyes and antibodies remains a challenge. Towards this goal, first, Tessier-Lavigne, Renier and colleagues developed iDISCO, which achieved immunolabelling of the adult mouse brain and allowed brain regions differentially activated during parenting behaviour to be uncovered[26]. iDISCO involves pretreatment of the specimen with solutions containing H_2O_2 and methanol to permeabilize mouse brain, a process that may also purge most of the epitopes for the antibodies[26]. In the future, development of new deep-tissue labelling approaches with full epitope preservation will be critical to broaden the applications of hydrophobic tissue-clearing methods.

To scale up the immunolabelling to whole adult mouse, Cai et al. recently introduced vDISCO (the 'v' refers to the variable domain of heavy-chain antibodies; that is, nanobodies), using high-pressure delivery of nanobodies for complete immunolabelling of the whole body with bright Atto dyes in the far-red region to overcome low signal intensity and autofluorescence of many tissues in the blue–green region[28]. This method amplified the fluorescent signal by two orders of magnitude and thereby allowed imaging of subcellular details and quantification of single cells deep in intact cleared mouse bodies through bones and muscles. vDISCO allowed the generation of the first whole-body neuronal projectome of adult mice, the study of neurodegeneration and inflammation throughout the body after CNS lesions and the co-discovery of skull–meninges connections, which seem to be critical for brain functions in physiological and pathological states[28,43]. As vDISCO enormously amplifies signal contrast even for dissected organs, in the future it will provide high-quality ground-truth data for machine learning-based algorithms aiming to map transgenically labelled mammalian brains[11,44].

Hydrophilic tissue clearing

Hydrophilic tissue-clearing methods use water-soluble reagents for tissue clearing. Although the tissue-clearing performance of hydrophilic tissue-clearing methods was sometimes inferior to that of hydrophobic tissue-clearing methods, the former have obvious advantages, including high levels of biocompatibility, biosafety and preservation of protein function. Hydrophilic reagents usually form hydrogen bonds with components of tissues such as proteins as well as surrounding water molecules, which can help to preserve the 3D structure of tissue components and, thereby, the signal of fluorescent proteins. Moreover, hydrophilic reagents can be dissolved in water at a high concentration and can be used as an RI-matching medium to provide a high RI in the medium. Hydrophilic tissue-clearing methods also have a long history of about a quarter of a century (since 1995; BOX 1).

One of the first applications of hydrophilic tissue clearing to neuroscience was by Chiang and colleagues. They developed FocusClear, which includes an X-ray contrast agent (for example, diatrizoate acid) and a detergent (for example, Tween 20), and applied it to imaging of a whole cockroach brain[45,46]. More recently, Miyawaki and colleagues developed Sca*l*e[12], which contains urea as a key tissue-clearing component, and can expand biological samples — for example, whole mouse embryos (embryonic day 13.5), infant mouse brains (postnatal day 15) and adult mouse brain slices (7–13 weeks old) — by hyperhydration[47] and thereby reduce their RIs. In contrast to most hydrophobic tissue-clearing regents, Sca*l*e can more efficiently preserve fluorescent proteins[12]. This method has allowed imaging of yellow fluorescent protein-labelled *Thy1*-expressing neurons in infant and adult mice, green fluorescent protein-labelled neural stem cells in the adult mouse hippocampus and cell-cycle status of mouse embryos via detection of the Fucci-S/G_2/M and Fucci-G_1/G_0 markers[12]. The researchers further developed Sca*l*e by

combining urea with sorbitol[48] to develop Sca*l*eS[49], which can be applied to adult, old and diseased mouse brain hemispheres. Imai and colleagues developed the See Deep Brain (SeeDB) protocol[13], which uses fructose[50] as its key RI-matching component, and used it to trace neural circuits in mouse olfactory bulbs because it does not expand or shrink biological samples and therefore preserves their morphology. They further refined this method by using an X-ray contrast agent with a higher RI, leading to the development of the SeeDB2 protocol, which has been applied to super-resolution imaging of neural circuits in mouse brains[51].

Ueda and colleagues took a system-level approach to identifying potent hydrophilic tissue-clearing reagents by comprehensive chemical profiling. They discovered a series of amino alcohols that have both delipidation[5] and decolourization[6] capabilities and then developed a series of clear, unobstructed brain or body imaging cocktails and computational analysis (CUBIC) reagents for both delipidation and decolourization[5,27,52]. Profiling more than 1,600 hydrophilic chemicals, they also discovered a series of aromatic amides that can be used as potent RI-matching reagents[22,27]. By combination of the most advanced delipidation (CUBIC-L, where 'L' stands for 'delipidation') and RI-matching (CUBIC-R+, where 'R' stands for 'RI matching' and '+' stands for a basic condition by adding an amino alcohol, *N*-butyldiethanolamine) reagents, the tissue-clearing performance of hydrophilic methods is now similar to or can even exceed that of hydrophobic methods without losing its advantages of biocompatibility, biosafety and preservation of protein function (for example, fluorescence)[22]. CUBIC has been applied to whole-brain imaging of immediate early gene expression induced by light exposure[5] and drug administration[53], whole-brain imaging of cancer metastasis[27], whole-brain imaging of individual neurons[54] and taste-sensing circuits in mouse brains[55], and 3D brain imaging of glutaminergic synaptic connections[56], hypothalamic neural subtypes[57], layer-specific astrocyte morphology[58] and visual projections of retinal ganglion cells[59]. CUBIC has been also applied to 3D imaging of other organs, including haematopoietic stem cells in bone marrow[60], carcinoma in the lung[61] and single-cell lineage tracing in the mammary gland[62] and development of a heart[63]. Therefore, the peripheral nervous systems in these organs can be analysed in detail.

Delipidation in some hydrophilic tissue-clearing methods creates space for large substances such as antibodies to penetrate more rapidly and deeply into tissues, allowing 3D immunohistochemistry in large samples. CUBIC has been successfully used to achieve 3D immunohistochemistry for adult mouse brain, heart, lung, stomach and intestine[5,6,22,27,52]. Recently, CUBIC-L–CUBIC-R was combined with whole-brain 3D immunohistochemistry to image blood vessels in entire mouse brains[27]. CUBIC was also applied to 3D immunohistochemistry and imaging of neurons expressing vesicular acetylcholine transporter that innervated islets in a pancreas[64]. In addition to the enhanced penetration of antibodies owing to delipidation, weakening the interaction between an antibody and a tissue seems to accelerate the penetration of an antibody into a tissue. For example,

Table 1 | **Tissue-clearing reagents used for whole-organ or body 3D imaging**

Chemical	Group	Role in tissue clearing	Cocktail or protocol	Refs
Methanol	Alcohol	Dehydration and permabilization	iDISCO, iDISCO+	4,8,26,36
Ethanol	Alcohol	Dehydration	BABB	14
tert-Butanol	Alcohol	Dehydration	FluoClearBABB, uDISCO, PEGASOS	42,169,170
Tetrahydrofuran	Ether	Dehydration	3DISCO, iDISCO, vDISCO	4,8,28,33,36,171
Benzyl alcohol	Aromatic alcohol	RI matching and delipidation (putative)	BABB, vDISCO	14,28,172
Benzyl benzoate	Aromatic ester	RI matching and delipidation (putative)	BABB, PEGASOS, vDISCO	14,28,170,172
Ethyl-3-phenylprop-2-enoate (ethyl cinnamate)	Aromatic ester	RI matching	Ethyl cinnamate method	11
Dibenzyl ether	Aromatic ether	RI matching and delipidation (putative)	3DISCO, iDISCO, iDISCO+	4,7,8,26,33,36,171,173
Diphenyl ether	Aromatic ether	RI matching and delipidation (putative)	uDISCO	42
Hexane	Alkane	Dehydration and delipidation?	BABB	14
Dichloromethane	Alkyl halide	Delipidation and dehydration	3DISCO, uDISCO, iDISCO, iDISCO+	4,8,26,33,36,42
Glycerol	Polyol	RI matching	Scale reagents, CLARITY, LUCID	12,174–179
2,2'-Thiodiethanol	Thioalcohol	RI matching	Single treatment, CLARITY, LUCID, TOMEI	10,161,177,178,180
Sucrose	Oligosaccharide	RI matching	ScaleCUBIC2, UbasM-2	5,6,52,181
D(−)-Fructose	Monosaccharide	RI matching	SeeDB, FRUIT	13,165
D(−)-Sorbitol	Monosaccharide	RI matching	sRIMS, ScaleS, STP tomography	3,49,54
Xylitol	Monosaccharide	Dehydration and RI matching	ClearSee	182
Methyl-β-cyclodextrin	Oligosaccharides	Delipidation (extracting cholesterol)	ScaleS, vDISCO	28,49
γ-Cyclodextrin	Oligosaccharides	Delipidation (extracting cholesterol)	ScaleS	49
Polyethylene glycol	Polyether	RI matching	Clear^{T2}, PEGASOS	163,170
Dimethyl sulfoxide	Sulfoxide	RI matching	ScaleS, STP tomography	49,50
Urea	Urea	Hydration (putatively contributes to expansion and hence RI matching) and chemical penetration	Scale reagents, ScaleCUBIC reagents UbasM, FRUIT, ClearSee, vDISCO	5,6,12,28,52,165,175, 176,179,181–183
1,3-Dimethyl-2-imidazolidinone	Urea	Hydration (putatively contributes to expansion and hence RI matching) and chemical penetration	UbasM-1–UbasM-2	181
Formamide	Amide	Putatively similar mechanism to urea	Clear^T, Clear^{T2}, RTF	162,184
N-Methylacetamide	Amide	RI matching	C$_e$3D	185
Nicotinamide	Aromatic amide	RI matching	CUBIC-R, CUBIC-R+	22,27
N-Methylnicotinamide	Aromatic amide	RI matching	CUBIC-R, CUBIC-R+	22,27
Antipyrine	Phenyl pyrazolone	RI matching and expansion	CUBIC-X, CUBIC-R, CUBIC-R+	17,22,27
5-(*N*-2,3-Dihydroxypropylacetamido)-2,4,6-triiodo-*N*,*N*'-bis(2,3-dihydroxypropyl) isophthalamide (iohexol)	Contrast reagent	RI matching	RIMS–SeeDB2–C$_e$3D	3,52,185
Diatrizoate acid	Contrast agent	RI matching	RI matching reagent in SWITCH protocol, FocusClear	2,25,47
Iodixanol	Contrast reagent	RI matching	RI matching reagent in SWITCH protocol	25
N-Acetyl-L-hydroxyproline (*trans*-1-acetyl-4-hydroxy-L-proline)	Amino acid	Relaxing collagen structure	ScaleS, vDISCO	28,49
N,*N*,*N*',*N*'-Tetrakis (2-hydroxypropyl) ethylenediamine (Quadrol)	Amino alcohol	Delipidation, decolorization and RI matching	ScaleCUBIC-1, PACT-deCAL–Bone CLARITY, PEGASOS, vDISCO	5,6,28,52,74,170
Triethanolamine	Amino alcohol	Delipidation, decolorization and RI matching	ScaleCUBIC-2, RTF	5,6,52,184

Table 1 (cont.) | **Tissue-clearing reagents used for whole-organ or body 3D imaging**

Chemical	Group	Role in tissue clearing	Cocktail or protocol	Refs
N-Butyldiethanolamine	Amino alcohol	Delipidation, decolorization and pH adjustment	CUBIC-L, CUBIC-R+	22,27
Meglumine or N-methyl-D-glucamine	Amino alcohol	Delipidation and RI matching	UbasM-1, RI matching reagent in SWITCH protocol	25,181
1,3-Bis(aminomethyl) cyclohexane	Aliphatic amine	Delipidation, decolorization and pH adjustment	CUBIC-HL	22
Imidazole	Imidazole	Expansion and decalcification (with EDTA)	CUBIC-X, CUBIC-B	17,22
1-Methylimidazole	Imidazole	Decolorization	CUBIC-P	22
Sodium dodecyl sulfate	Ionic detergent	Delipidation	CLARITY and related protocols (PACT, PARS, ACT, FACT, FASTClear and simplified CLARITY), SWITCH	2,3,9,10,22,25,67,74, 89,174,183,186–188
Sodium dodecylbenzenesulfonate	Ionic detergent	Delipidation	CUBIC-HL	22
Sodium deoxycholate	Ionic detergent	Delipidation	ClearSee	182
Triton X-100	Non-ionic detergent	Delipidation	Scale reagents, ScaleCUBIC-1, UbasM-1 (0.2%), C_e3D (0.1%), SUT, CUBIC-L, CUBIC-HL, vDISCO	5,6,12,22,28,52,175, 176,181,183,185
Tween 20	Non-ionic detergent	Delipidation	FocusClear	47
EDTA	EDTA	Decalcification	PACT-deCal, Bone CLARITY, CUBIC-B, PEGASOS, vDISCO	9,22,28,74,170

BABB, benzyl alcohol and benzyl benzoate; C_e3D, clearing-enhanced 3D; EDTA, ethylenediaminetetraacetic acid; FACT, fast free-of-acrylamide clearing tissue; LUCID, illuminate cleared organs to identify target molecules; PEGASOS, polyethylene glycol-associated solvent system; RTF, rapid clearing method based on triethanolamine and formamide; RI, refractive index; RIMS, refractive index-matching solution; STP tomography, serial two-photon tomography; TOMEI, transparent plant organ method for imaging; UbasM, urea-based amino-sugar mixture.

the AbScale protocol, which uses the protein denaturant urea in antibody staining, achieved 3D immunohistochemistry of an adult mouse hemisphere[49]. An original Scale protocol uses urea for tissue clearing not for antibody staining. AbScale was used with brain-wide immunohistochemistry to image amyloid-β plaques, a hallmark pathological feature of Alzheimer disease, in mice[27,49].

Hydrophilic methods can be also extended to expansion microscopy[65]. For example, the CUBIC-X protocol, which involves the use of an imidazole and an antipyrine as hyperhydrating reagents, can expand the adult mouse brain 10-fold in volume[17] (the 'X' in CUBIC-X stands for 'X-fold expansion'). The use of the CUBIC-X protocol allows whole-brain cell profiling of adult mouse brains and allowed the development of a 3D single-cell-resolution mouse brain atlas (CUBIC-Atlas)[17], which contains ~10^8 cells of an entire brain[17,66] (FIG. 2). Such brain atlases could become widely used platforms for mapping cell activity (for example, the expression of immediate early genes), cell types (for example, specific subtypes of neurons and glia cells) and neural connectomes (for example, mapping the neural connections by adeno-associated virus and/or rabies virus).

Hydrogel-based tissue clearing

To widen the applications of tissue-clearing technologies, Deisseroth, Chung and colleagues introduced a hydrogel-based tissue-clearing method called 'cleared lipid-extracted acryl-hybridized rigid immunostaining/in situ hybridization-compatible tissue hydrogel' (CLARI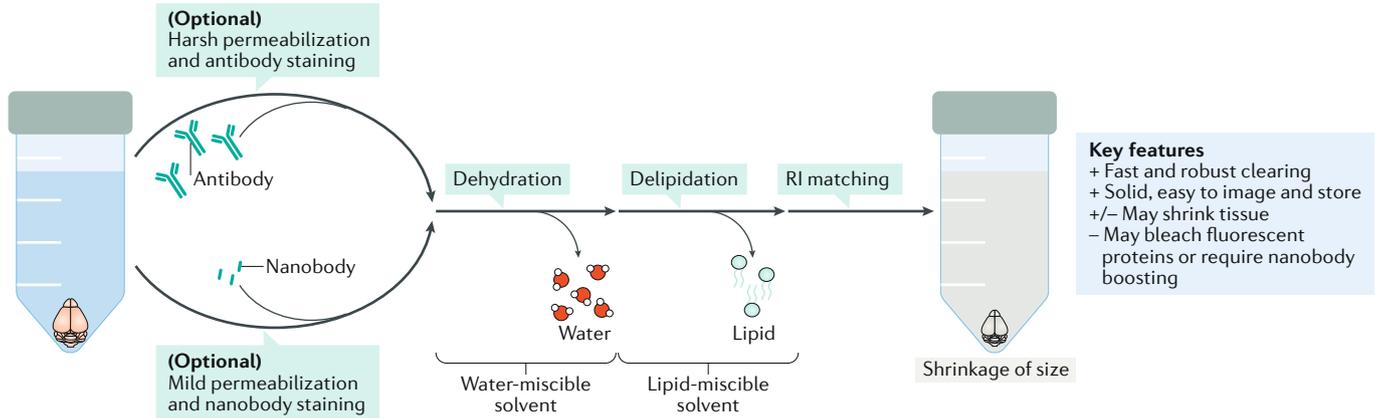TY), which secures a broad category of biomolecules at their physiological locations by covalently linking the molecules to an acryl-based hydrogel[2] (FIG. 3). This unique hydrogel reinforcement allows complete and uniform removal of lipids from the tissue while minimizing structural damage and loss of biomolecules (10% protein loss in CLARITY versus 70% protein loss in formaldehyde-only fixed tissues)[2]. In CLARITY, both electrophoresis-driven and simple passive clearing can effectively remove lipids, which drastically increases the optical transparency and macromolecule permeability of the hydrogel–tissue hybrid[2]. The cleared intact organs can be imaged by fluorescence microscopy without loss of resolution. Small tissues can be readily stained with molecular probes (such as antibodies); however, the staining of large tissues requires longer incubation times as in all the tissue-processing methods that rely on passive diffusion.

Variants of CLARITY[3,9,67,68] have been developed to increase tissue permeability and probe penetration by decreasing gel density and the degree of crosslinking, such as the passive CLARITY technique (PACT)[3,67]. Weakening gel architecture, however, causes loss of tissue information. To accelerate molecular labelling without compromising tissue integrity, a new mode of transporting molecules into tissue was developed, termed 'stochastic electrotransport'. Stochastic electrotransport generates electrophoretically driven diffusive random motion of a broad range of molecules (for example, antibodies, dyes and detergents) to rapidly deliver them into dense tissue gels and it allows uniform clearing and staining of intact mouse organs within 2 or 3 days (as opposed to weeks to months in methods that rely on the passive diffusion of such molecules)[24].
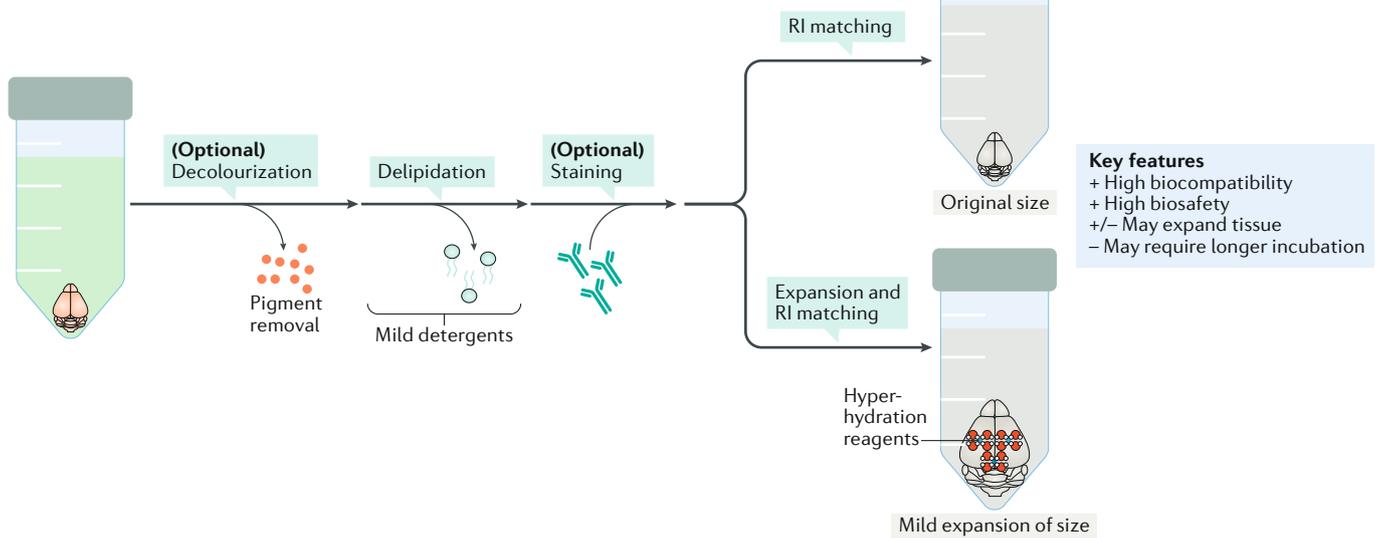
Passive CLARITY technique (PACT). A technique that allows flexible hydrogel formulation and clearing without the need to use electrophoresis.
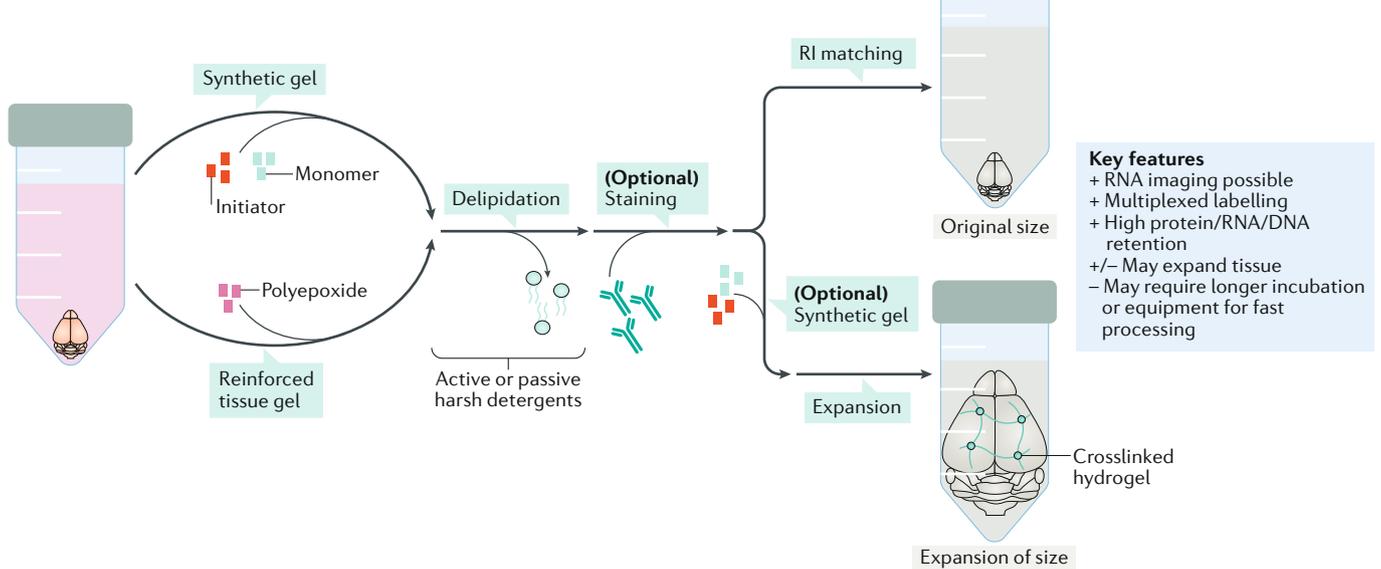
a Hydrophobic method

(Optional)
Harsh permeabilization
and antibody staining

Antibody

Nanobody

(Optional)
Mild permeabilization
and nanobody staining

Dehydration

Delipidation

RI matching

Water

Lipid

Water-miscible
solvent

Lipid-miscible
solvent

Shrinkage of size

Key features
+ Fast and robust clearing
+ Solid, easy to image and store
+/− May shrink tissue
− May bleach fluorescent
  proteins or require nanobody
  boosting

b Hydrophilic method

(Optional)
Decolourization

Delipidation

(Optional)
Staining

Pigment
removal

Mild detergents

RI matching

Original size

Expansion and
RI matching

Hyper-
hydration
reagents

Mild expansion of size

Key features
+ High biocompatibility
+ High biosafety
+/− May expand tissue
− May require longer incubation

c Hydrogel-based method

Synthetic gel

Monomer

Initiator

Polyepoxide

Reinforced
tissue gel

Delipidation

(Optional)
Staining

Active or passive
harsh detergents

RI matching

Original size

(Optional)
Synthetic gel

Expansion

Crosslinked
hydrogel

Expansion of size

Key features
+ RNA imaging possible
+ Multiplexed labelling
+ High protein/RNA/DNA
  retention
+/− May expand tissue
− May require longer incubation
  or equipment for fast
  processing

Fig. 1 | **Major tissue-clearing methods and their key features. a** | Hydrophobic methods rely on a complete dehydration of the tissue, followed by lipid extraction and refractive index (RI) matching using organic solvents. Hydrophobic methods are generally fast and can clear tissues fully. However, some hydrophobic methods can bleach the signal of fluorescent proteins rapidly. **b** | Hydrophilic methods are based on water-soluble solutions and are usually associated with higher biosafety and compatibility than hydrophobic methods. A potent hydrophilic method such as CUBIC starts with decolourization, which is followed by delipidation, RI matching and (optionally) expansion; some hydrophilic methods need longer incubation times for intact organs. **c** | Hydrogel embedding forms the third major category of tissue clearing. Hydrogel-based methods use either monomer and initiator molecules to make a synthetic gel or polyepoxide to make a reinforced tissue gel. Hydrogel-based methods can allow retainment of enough RNAs for assays such as fluorescence in situ hybridization and can be used to expand tissues severalfold owing to the hydrogel mesh that glues the tissues. Some hydrogel-based methods need longer incubation times for intact organs.

Refractive index-matching solution
A solution that is compatible with the passive CLARITY technique, perfusion-assisted agent release in situ and CLARITY. It provides high-resolution imaging at depth by further reducing light scattering in both cleared and uncleared samples.

The physicochemical properties of the acryl-based gel can be engineered to add functionalities to the tissue–gel hybrid. Boyden and colleagues hybridized tissue with an expandable hydrogel and then digested proteins using a proteinase to expand the construct isotropically for super-resolution imaging[65]. Chung and colleagues developed a technique called 'magnified analysis of proteome' (MAP) that eliminated the protein digestion step described above to preserve the 3D proteome of intact organs while allowing isotropic expansion[69]. In MAP, a highly dense hydrogel is synthesized in situ and then protein complexes are dissociated to achieve isotropic expansion of the 3D proteome at the organ level. The authors

demonstrated its distinct utility for super-resolution imaging and reconstruction of neural projections. For better RNA detection, a recent study used 1-ethyl-3-(3-dimethylaminopropyl)carbodiimide chemistry to anchor RNAs to polyacrylamide gel[70].

These technological advances have allowed the brain-wide spatial mapping of biomolecules at subcellular resolution. However, the harsh chemical processing used in many tissue-clearing methods, such as detergent and organic solvent treatments, sometimes cause tissue damage. To address this limitation, a method termed 'stabilization to harsh conditions via intramolecular epoxide linkages to prevent degradation' (SHIELD) was developed to preserve the fluorescence of proteins, protein antigenicity, transcripts and tissue architecture in organ-scale transparent tissues. SHIELD uses polyepoxy chemicals to protect the physicochemical properties (for example, protein fluorescence and antigenicity) of biomolecules by forming intramolecular and inte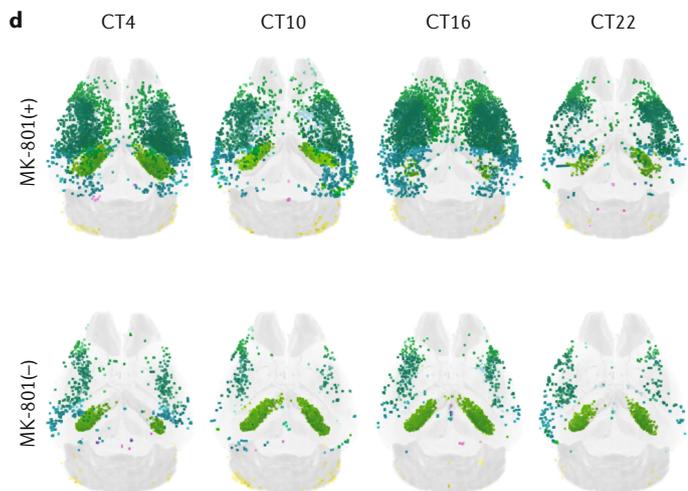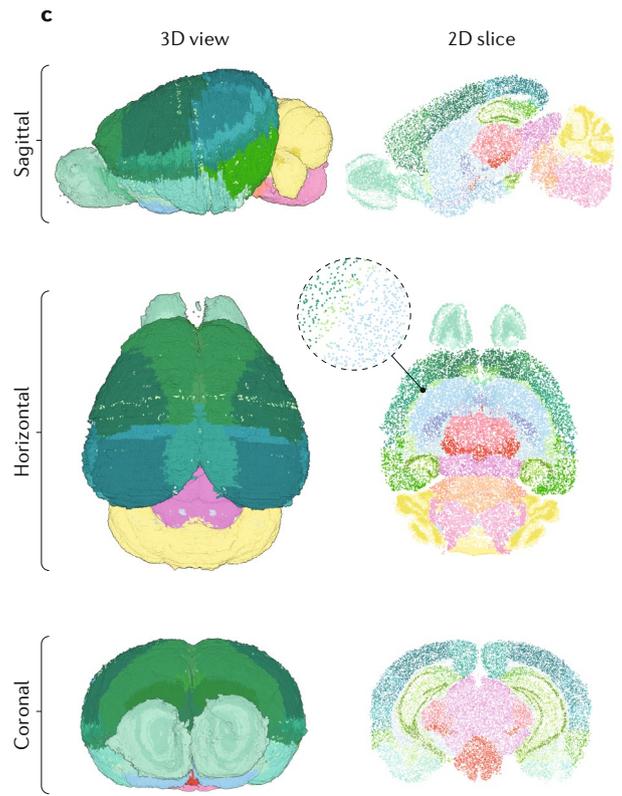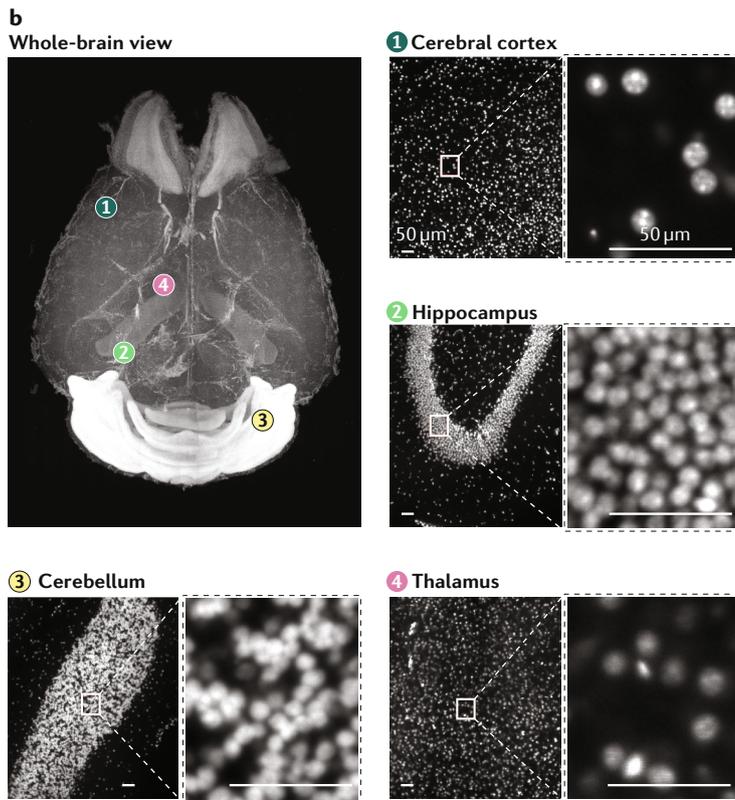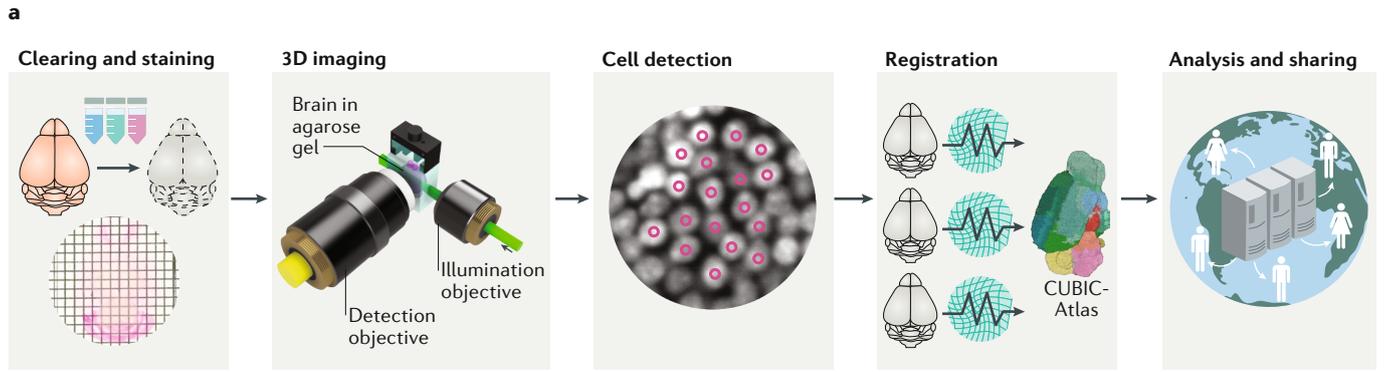rmolecular crosslinks[71]. To achieve uniform and controlled crosslinking in organ-scale tissues, polyepoxy chemicals are first dispersed in a buffer called 'system-wide control of interaction time and kinetics of chemicals (SWITCH)-Off buffer' that inhibits the fixation reaction[25]. Once the crosslinker has been uniformly dispersed, the reaction is turned on globally by moving the sample to a SWITCH-On buffer that enhances the fixation reaction. This simple strategy allowed scalable and uniform preservation of protein fluorescence, transcripts and proteins. SHIELD-preserved and delipidated tissue can withstand harsh antibody destaining conditions and therefore allows multiple rounds of staining and imaging of the same sample. Using SHIELD, the study authors demonstrated integrated mapping of neural circuits and their downstream targets at single-cell resolution as well as 3D molecular phenotyping of intact needle biopsy samples within only hours[25] (FIG. 3). In addition, these technologies have allowed the study of 3D structure of cerebral organoids[72] and network-specific amyloid progression[73].

Hydrogel-based methods are further applicable to the whole-body scale. Gradinaru and colleagues developed perfusion-assisted agent release in situ (PARS), which rendered rodent bodies transparent, allowing maps of central and peripheral nerves at target organs to be obtained[3,68]. Gradinaru and colleagues realized that the circulatory system (the vasculature) could be used to deliver clearing agents and labels instead of relying on passive diffusion, which is prohibitively slow for large organs or whole organisms. CLARITY-based methods[2] can be adapted for bones[74], and for magnified single-cell visualization while retaining fluorescent markers (see Supplementary Fig. 4 in REF.[9]).

Labelling
For CLARITY and other tissue-clearing methods to reach their full potential, it will be imperative to integrate data from post-mortem samples with markers of functionality. We cannot remove the lipids while keeping the brain alive, but we can at least store a short-term 'memory of neuronal activity' via transcriptional or biochemical changes (for example, Ca^{2+} influx) that can be evaluated after death and brain-wide. The history of

a

Clearing and staining | 3D imaging | Cell detection | Registration | Analysis and sharing

Brain in agarose gel

Detection objective

Illumination objective

CUBIC-Atlas

b

Whole-brain view

① Cerebral cortex

50 μm / 50 μm

② Hippocampus

③ Cerebellum

④ Thalamus

c

3D view | 2D slice

Sagittal

Horizontal

Coronal

d

CT4 | CT10 | CT16 | CT22

MK-801(+)

MK-801(−)

e

Cluster 1 | Cluster 2 | Cluster 3 | Cluster 4

Coronal sections

Section 1

Section 2

Section 3

Fig. 2 | **Whole-brain single-cell-resolution imaging and analysis. a** | Tissue-clearing methods allow whole-brain profiling of cells. The brain data obtained can be registered in the 3D single-cell-resolution mouse brain atlas (CUBIC-Atlas) and shared by a worldwide research community via the Internet[17]. First, tissue clearing (and fluorescent staining if applicable) is applied to the specimen. Cleared brains are imaged using high-resolution light-sheet microscopy. A graphics processing unit-based high-speed cell counting program identifies all cells from the acquired images, rendering the whole tissue into an ensemble of cellular points (that is, a point cloud). Then, individual brains are registered onto the common brain coordinates to allow quantitative comparison and analysis. Finally, these data should be shared among researchers to allow collaborative and large-scale analysis. **b** | Images of an adult mouse brain obtained by the hydrophilic tissue-clearing and expansion protocol CUBIC-X and custom-made high-resolution light-sheet microscopy[17]. Nuclear staining using propidium iodide was applied to the cleared brain tissue. Magnified views of some of the representative brain regions, including cerebral cortex (view 1), hippocampus (view 2), cerebellum (view 3) and thalamus (view 4), are presented, along with the whole-brain overview. Scale bars indicate 50 μm after normalization of the sample expansion. **c** | The 3D single-cell-resolution mouse brain atlas CUBIC-Atlas. With use of nuclear staining images such as the ones shown in part **b**, all cell nuclei in a whole mouse brain were identified, totalling ~10^8 cells[17,66]. The colour of each cell represents anatomical annotations of each brain region obtained from the Allen Brain Atlas. **d** | The whole-brain neuronal activity profile with or without the long-term administration of a NMDA receptor inhibitor (MK-801) was quantified by imaging the destabilized fluorescent protein dVenus under the control of the *Arc* gene promoter by using the Arc–dVenus transgenic mouse[53]. Each Arc–dVenus mouse brain at different circadian times (CT) was mapped onto CUBIC-Atlas in a probabilistic manner to virtually reconstruct the time series[17]. Arc–dVenus-expressing cells are shown as dots, with their colours representing their anatomical areas. **e** | By clustering analysis of the data shown in part **d**, four distinct populations of cells were identified, exhibiting different activity patterns on MK-801 administration. Localization of each cluster is shown in coronal sections, revealing an inhomogeneous cellular population in the lower and upper dentate gyrus. Parts **b–e** were adapted from REF.[17], Springer Nature Limited.

Perfusion-assisted agent release in situ
(PARS). A method that allows whole-rodent clearing and labelling. It uses the intrinsic circulatory system (the vasculature) to deliver clearing agents and labels instead of relying on passive diffusion, which can be prohibitively slow for large organs or whole organisms.

Hydrogel-based tissue clearing
One of three major tissue-clearing methods; it crosslinks biological specimens to make a synthetic hydrogel.

activity in brain circuits can also be reported by changes in protein expression. As discussed earlier, hydrophobic, hydrophilic and hydrogel-based tissue-clearing methods are compatible with antibody staining of intact organs. The legacy of brain activity is also reported by changes in RNA transcripts, which can be detected by single-molecule fluorescence in situ hybridization and are indeed retained in PACT-cleared tissues[3,75]. More broadly, preserving the spatial relationships of tissues while accessing the transcriptome of selected cells is of crucial interest for many areas of biology and it motivated the development of methods for multicolour, multi-RNA imaging in deep tissue[71]. With use of single-molecule hybridization chain reaction, tissue hydrogel embedding and clearing by PACT and light-sheet microscopy, the detection of single-molecule mRNAs in approximately millimetre-thick brain slices is possible[76]. With rRNA labelling in PACT-cleared samples, researchers mapped the identity and growth rate of pathogens in sputum samples from individuals with cystic fibrosis[77].

Tissue-clearing methods have been particularly useful in tracing long-range projections in the CNS and the peripheral nervous system. However, to maximize their impact, the clearing methods need to be complemented by labelling methods that can, for example, highlight the desired circuits with strong, morphology-filling markers, while preserving their genetic identity and be easy to use and highly customizable (that is, they minimize the need to generate or cross transgenic animals)[78]. This has been nicely applied to study the topography of dopaminergic projections in the mouse brain[79].

As morphology reconstruction is difficult in data sets from densely labelled neurons, it would be desirable for the fraction of cells labelled to be easily controlled. Recruiting the power of recently engineered systemic adeno-associated viruses that can cross the blood–brain barrier[29,80] has been beneficial in this respect, and methods are now available to label individual cells in the brain, peripheral nervous system and other organs with a wide range of hues using genetically encoded fluorescent proteins expressed by multiple viral vectors. Viral-assisted spectral tracing is a highly customizable multicolour labelling system with controlled labelling density that allows detailed studies of the 3D morphology of cells in intact, thick, cleared tissue samples (FIG. 3). The unique power of a labelling approach based on gene delivery is that in addition to it providing morphology markers, one can introduce state-altering genes and evaluate the effects on morphology of state-modified and state-unmodified cells within the same subject; coupled with tissue clearing, this will greatly enhance our understanding of physiology and pathology[81].
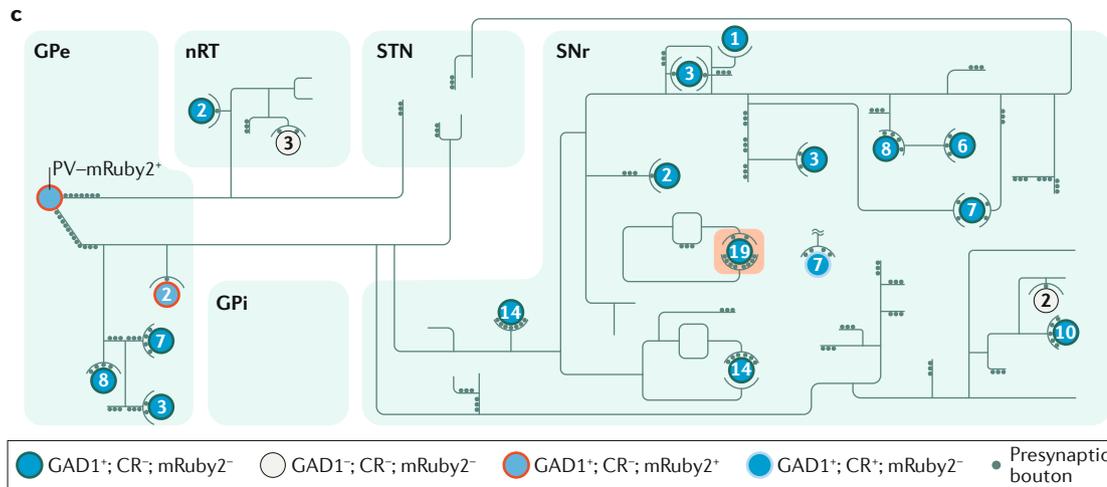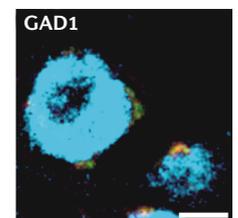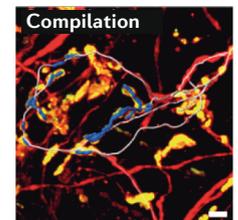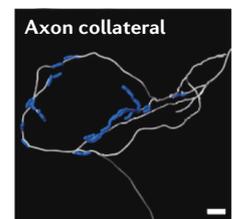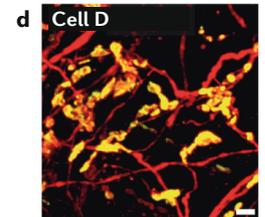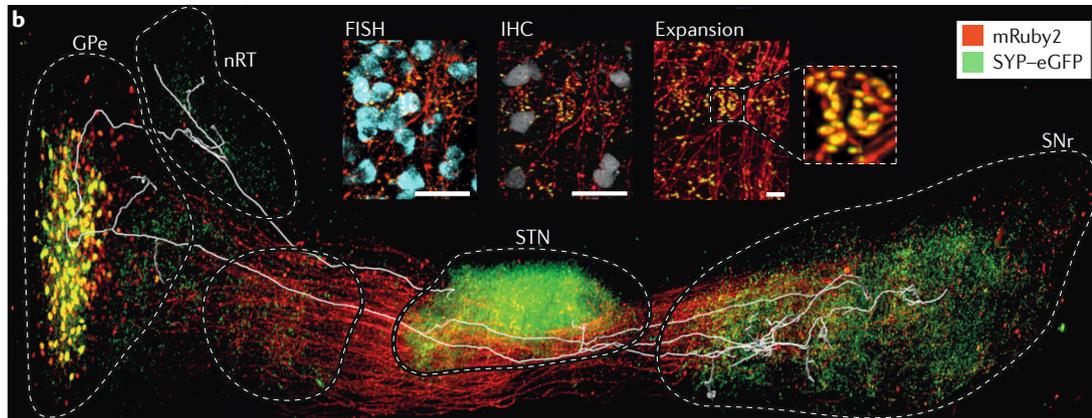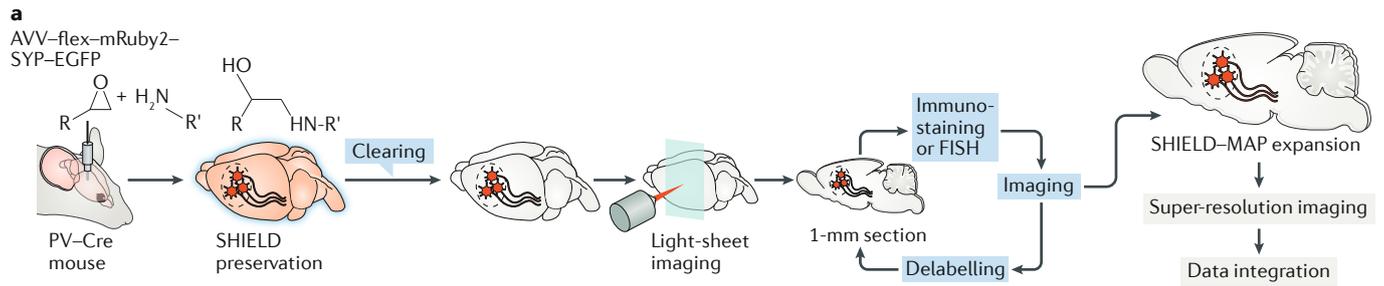
Applications in humans

Our knowledge of the human body is primarily macroscopic and based on classic anatomical methods that were established centuries ago and that require the dissection and slicing of individual organs such as the brain. However, recent studies have showed that tissue clearing and light-sheet microscopy are starting to revolutionize not only the study of experimental animals but also the study of the anatomy of and disease diagnosis in humans. The surge of tissue-clearing innovation comes primarily from neurobiologists, who are facing a daunting task: deciphering the human connectome. The nervous system is by far the most complex organ, with probably hundreds of different cell types forming intricate circuits and networks, the organization of which is extremely difficult to understand from 2D slices. The combination of tissue clearing and light-sheet microscopy has already allowed us to image entire mouse brains and spinal cords and to better understand the extent of CNS deterioration in some animal models of neurological diseases[8,26,82,83]. The CUBIC approach has been combined with stimulated emission depletion microscopy to better visualize synaptic contacts onto the dendritic spines of pyramidal neurons in the mouse cortex[84]. The next challenge is to translate this knowledge to the analysis of the human nervous system and to develop applications that will improve the post-mortem pathological evaluation of brain disorders.

CLARITY-based clearing procedures have allowed successful imaging of cortical pyramidal neurons and interneurons[85,86] and cerebellar Purkinje cells and granule cells[87] in healthy human brain samples. Such procedures have also permitted imaging of pathological human brain samples, including visualization of tissue from an individual with autism[2], α-synuclein inclusions, dopaminergic axons and substantia nigra in Parkinson disease[88], Purkinje cells, mitochondria and vasculature in cerebellar ataxia[87] and amyloid plaques in Alzheimer disease[85]. Other brain-clearing techniques,

a

AVV–flex–mRuby2–SYP–EGFP

PV–Cre mouse → SHIELD preservation → Clearing → Light-sheet imaging → 1-mm section → Immuno-staining or FISH → Imaging → Delabelling → SHIELD–MAP expansion → Super-resolution imaging → Data integration

b

GPe, nRT, SNr, STN

FISH, IHC, Expansion

mRuby2 / SYP–eGFP

c

GPe, nRT, STN, SNr, GPi

PV–mRuby2+

GAD1+; CR−; mRuby2−   GAD1−; CR−; mRuby2−   GAD1+; CR−; mRuby2+   GAD1+; CR+; mRuby2−   Presynaptic bouton

d

Cell D

Axon collateral

Compilation

GAD1

e Two-component AAV-based multicolour sparse labelling system

Variable-dose inducer virus

hSyn1 | Inducible

High-dose three-colour cocktail

Inducible | | WPRE
Inducible | | WPRE
Inducible | | WPRE

f

Projection image   Traced morphology   Overlay

◀ Fig. 3 | **The SHIELD–MAP and AAV-based labelling system.** SHIELD (system-wide control of interaction time and kinetics of chemicals) combined with MAP (magnified analysis of proteome) allows integrated circuit mapping at single-cell resolution. **a** | The SHIELD–MAP pipeline. SHIELD allows fully integrated multiscale imaging of fluorescent protein-labelled circuits, mRNAs and proteins within the same mouse brain by simultaneously protecting the molecular and structural information within cleared tissues. **b** | The image shows a 3D rendering of fluorescent protein-labelled neuronal circuitry of parvalbumin (PV)-positive neurons in the globus pallidus externa (GPe) with an overlaid axon trace of a single labelled neuron. The inset shows example images from multiround staining and multiscale imaging. Scale bar 50 μm for the insets. **c** | Reconstructed axon arborization of the neuron and its downstream targets. Each circle represents a neuron. The number of putative axosomatic boutons is marked inside each circle. The colour of each circle provides molecular details for each neuron. **d** | Reconstructed putative axosomatic connectivity for 'cell D' (the cell highlighted in orange in part **c**). Ramified axons (grey) and enhanced green fluorescent protein (eGFP)-positive presynaptic boutons (blue) are segmented[71]. Scale bars 20 μm. **e** | Viral-assisted spectral tracing (VAST) can be used to label and visualize the 3D morphology and connectivity of cells in thick, cleared tissue blocks. Here, the schematic shows the two-component VAST labelling system[30,80,122]. A high dose of a three-vector cocktail (individually expressing a red, green or blue fluorescent protein) is coadministered along with a variable dose of an inducer vector that is required to turn on expression of the three proteins. To label specific cell populations, the expression of the fluorescent proteins can also be made Cre dependent. **f** | Projection image of the olfactory bulb where mitral cells are labelled by VAST (left). Sparse labelling of these cells allows tracing of their dendritic arbors (middle). An overlay of the traces and the projection image is shown in right-hand image. AAV, adeno-associated virus; CR, calretinin; FISH, fluorescence in situ hybridization; hSyn1, human synapsin 1 gene promoter; IHC, immunohistochemistry; GPi, globus pallidus interna; nRT, nucleus reticularis thalami; SNr, substantia nigra pars reticulata; STN, subthalamic nucleus; WPRE, Woodchuck hepatitis post-transcriptional regulatory element. Parts **a**–**d** are adapted from REF.[71], Springer Nature Limited. Parts **e** and **f** are adapted from REF.[80], Springer Nature Limited.

such as iDISCO[82] and ScaleS[49], have also been tried on Alzheimer disease brain samples; although confirmatory, these studies provided more direct evidence for an association between microglia and amyloid plaques, with these techniques also facilitating the detection of diffuse plaques. CUBIC[27] has been used in whole-brain immunohistochemistry of blood vessels in cancer metastasis. Moreover, GABAergic interneurons were imaged in slices from hemimegalencephalic cortex that was cleared with 2,2′-thiodiethanol[10], and neurons and vessels were imaged in spinal cord fragments that were cleared with ACT-PRESTO (active clarity technique–pressure-related efficient and stable transfer of macromolecules into organs)[89]. The clearing reagent OPTIClear[90] is compatible with lipophilic dyes and has been used to label mossy fibre axons in adult human cerebellum.

Together, the studies mentioned above provide proof of concept for and support the feasibility of human brain clearing, but these and other studies illustrate the current technical limitations of this approach in humans. First, clearing was efficient on relatively thin brain slices or blocks of no more than a few hundred cubic micrometres[2,25,49,82,85,87,88,90], corresponding at best to about 1/1,500 of the total human brain volume[91]. Good transparency sometimes required a significant extension of the clearing time, compared with a few days in rodents[10]. Second, formalin-fixed human brain tissue is highly autofluorescent, is rich in blood and contains lipofuscin-type pigments and neuromelanin, which are very difficult to clear. Third, immunostaining was successful only on samples thinner than a few hundred micrometres, and many antibodies failed to work following tissue-clearing

treatment. Using single-chain variable fragments of conventional antibodies or nanobodies might be a good option to increase penetration into the brain samples[92]. Therefore, although the progress so far is promising, routine post-mortem 3D imaging of the entire human brain is still currently out of reach and remains a tantalizing challenge. Scalability of the clearing method will be essential, and there is also a need to develop light-sheet microscopes with much longer working distances and a larger field of view. Solvent-based clearing methods, which can drastically reduce the sample volume, might then be preferred. When optimized, human brain clearing will be a unique tool for correlating and validating in vivo 3D data obtained by MRI and diffusion tensor imaging. This will be essential to improve the diagnosis of disease.

Although 3D imaging of transparent adult human CNS is still in its infancy, tissue clearing has already provided a wealth of new information in the field of human embryology and allows easy access to 3D cytoarchitecture of millimetre-sized brain organoids[92]. Solvent-based DISCO clearing methods proved to be perfectly adapted to the transparentization of human embryos and fetuses at least up to 3 months of gestation[23,93]. Moreover, with use of this approach, whole-mount immunolabelling of centimetre-sized human specimens was performed with a large panel of antibodies[23] (FIG. 4), and indicated how motor and sensory axons invade the hands, limbs, head and various organs and revealed an unexpected heterogeneity and stochasticity of sensory nerve branching pattern[23]. 3D imaging of DISCO-cleared human embryos also demonstrated that neurons secreting gonadotropin-releasing hormone migrate in two separate pathways and colonize many brain regions outside the hypothalamus[93]. The innervation of the embryonic pancreas was described following the use of CLARITY[94]. One can now revisit embryology and envisage building a comprehensive 3D cartography of human development. Indeed, tissue clearing will be extremely valuable to the Human Developmental Cell Atlas project[95], one component of the Human Cell Atlas, an international initiative that aims to identify and map all cells of the human body.

Understanding how tumour cells and viruses proliferate and spread within the body are major questions in oncology and virology, and they are attracting greater attention[96] in neuroscience because there are tight interactions between nervous systems and the immune system[97]. Recent applications of tissue-clearing methods have helped follow at an unprecedented resolution the dissemination of HIV-infected human T lymphocytes in mouse lymphoid organs[96] and human cancer cell lines in whole cleared mice[27]. These studies have already demonstrated that the cellular resolution in cleared organs significantly outperforms what is achieved with classic tumour detection methods such as bioluminescence. The cellular composition of cleared human tumour biopsy samples has also been described[94,98–100]. Therefore, once adopted by histopathologists, tissue clearing is expected to rapidly improve the analysis of tumour cell niches in their native context, diagnosis, staging of tumours and the validation of anticancer and antiviral therapies.

Light-sheet microscopy

To take full advantage of the clearing methods discussed so far and systematically extract structural information at the subcellular level, clearing methods require microscopes that are capable of rapid, high-resolution imaging of large volumes. Several powerful imaging methods have been developed or adapted for this purpose. Some of these efforts focused on pushing existing, well-established techniques, such as two-photon microscopy, to their performance limits. Notably, Chandrashekar, Myers and colleagues developed an entire imaging framework that integrates a fast, resonant-scanning two-photon microscope with a tissue vibratome to facilitate whole-brain imaging at high spatial resolution[54]. They achieved a spatial resolution of 0.45 μm laterally and 1.33 μm axially at a data acquisition rate of 1.6×10^6 μm³ per second (FIG. 5), which allowed the fully automated acquisition of entire mouse brains in approximately 1 week. To increase the speed and resolution even further, ongoing efforts are taking advantage of emerging imaging strategies. Light-sheet microscopy[101–103] is a key approach to this end, as it promises particularly striking performance advances in both spatial and temporal regimes.

The central idea in light-sheet microscopy is to illuminate the specimen with a thin sheet of laser light from the side and acquire an image of the illuminated plane with a camera-based detection system. In the most common implementations of light-sheet microscopy, the wide-field detection arm is oriented at a right angle to the light-sheet illumination axis and separate objectives are used for illumination and detection. Compared with conventional microscopy, this approach offers two primary advantages for the imaging of large tissue volumes. First, the imaging speed is limited only by the acquisition rate of the camera and thus exceptionally high data rates of up to several hundred million voxels per second can be achieved with state-of-the-art sCMOS detectors. Second, photobleaching and phototoxic effects are kept to a minimum, since only the plane in the focus of the detection system is illuminated with laser light. The amount of energy any part of the sample is exposed to is thus constant and independent of the total size of the sample or imaging volume. By contrast, conventional or confocal microscopes, which use the same objective for illumination and detection, illuminate also out-of-focus regions in the imaging process (above and below the focal plane). In these latter methods, local light exposure thus increases linearly with the size of the imaging volume and can even result in complete bleaching of parts of the specimen before volume acquisition is complete.

Shortly after its modern reincarnation at the beginning of this century, light-sheet microscopy was first applied to the imaging of cleared tissues in 2007 by Dodt and colleagues[14]. To rapidly acquire volumetric image data from fluorescently labelled, excised hippocampi and even whole embryonic mouse brains, they developed a light-sheet microscope with low-magnification, long-working-distance detection optics and two opposing illumination arms. This approach offered a spatial resolution on the order of several μm axially and slightly less than 1 μm laterally (FIG. 5). Since this first report, many other studies have used light-sheet imaging for conceptually similar experiments. Initial efforts relied exclusively on custom-built systems[67,104–108], but soon thereafter the first commercial products followed, such as the LaVision BioTec ultramicroscope[5,6,8,23,33,42,52]. These microscopes were quickly made compatible with a variety of clearing methods and a wide spectrum of biological specimens, including various organs[2,5,7,33], whole rat brains[107], chicken embryos[106], human embryos[23] and even entire adult mice[3,6,42].

Imaging speed in light-sheet microscopy is generally limited by the frame rate of the camera, and most approaches use similar optics and similar types of static[101] or scanned[102] light sheets. Therefore, comparable spatial and temporal resolutions have been achieved with most systems developed and used to date. Importantly, however, in the past few years, new approaches have allowed fundamental advances in spatial resolution in light-sheet microscopes designed for live imaging applications. When a relatively large field of view is being imaged, the resolution in standard light-sheet microscopy is comparably low along the direction of the detection axis — typically several μm at best. This limitation arises from the relatively thick light sheets that are generated by conventional beam-shaping techniques. By contrast, high, spatially isotropic resolution of about a few hundred nm can now be achieved using Bessel beams[109] or lattice light-sheets[110], which present an alternative to conventionally used Gaussian beams

Fig. 4 | **Towards a 3D developmental human cell atlas.** Solvent-based tissue clearing is particularly suitable for the analysis of human embryos as it allows visualization and mapping of immunolabelled cells in large and intact specimens. This provides unprecedented views of developing organs and human cells. **a–d** | Peripheral nerves (part **a**), Müllerian and Wolffian ducts and kidney in the urogenital system (part **b**), muscles in the back, arm and head (part **c**) and the vasculature in the hand (part **d**) of a human embryo at 8 weeks of gestation. **e,f** | The three sensory nerves of the hand (part **e**) and lung epithelial tubules (part **f**) in a fetus at 9.5 weeks of gestation. Parts **a,b,d–f** are adapted with permission from REF.[23], Elsevier. Part **c** is adapted with permission from REF.[165], Company of Biologists doi:10.1242/dev.180349.

a

Axial system resolution (μm)

- LLS SI (Chen et al. (2014))
- diSPIM (Wu et al. (2013))
- IsoView (Chhetri et al. (2015))
- LLS dithered (Chen et al. (2014))
- Two-photon (Economo et al. (2016))
- Zeiss Lightsheet Z.1
- Ultramicroscopy (Dodt et al. (2007))
- LaVision BioTec ultramicroscope
- SPED (Tomer et al. (2015))

Lateral system resolution (μm)

b

Volume throughput (μm³ s⁻¹)

- LaVision BioTec ultramicroscope (×1.26)
- SPED (Tomer et al. (2015))
- IsoView (Chhetri et al. ((2015)) (×16)
- LaVision BioTec ultramicroscope (×12.6)
- IsoView (Chhetri et al. (2015)) (×32)
- Two-photon (Economo et al. (2016))
- Zeiss Lightsheet Z.1
- Ultramicroscopy (Dodt et al. (2007))
- diSPIM (Wu et al. (2013))
- LLS dithered (Chen et al. (2014))

Sampling-limited 3D resolution (μm³)

c

- Two-photon (Economo et al. (2016))
- LLS (Chen et al. (2014))
- diSPIM (Wu et al. (2013))
- Zeiss Lightsheet Z.1
- IsoView (Chhetri et al. (2015))
- Ultramicroscopy (Dodt et al. (2007))
- LaVision BioTec ultramicroscope

Working distance (mm)

Fig. 5 | **Resolution and speed of custom and commercial light-sheet microscopes. a** | Lateral versus axial system resolution of custom[14,105,110–112] (red) and commercial[166,167] (green) light-sheet microscopes and state-of-the-art two-photon microscopes[54] (blue). System resolution values[168] represent the optical configurations and light-sheet properties reported in each study for the demonstration experiments shown in part **b**. The quantification disregards spatial sampling limitations inherent to the choice of detector. Resolution values are provided as the full width at half maximum (FWHM) size of the system point spread function. Lattice light-sheet (LLS) microscopy uses two different acquisition modes (dithered light sheet versus structured illumination (SI)), which affect the speed and resolution. **b** | Sampling-limited 3D resolution versus volume throughput for commercial light-sheet microscopes (green) and imaging experiments performed with custom light-sheet (black) and two-photon (blue) microscopes. 3D resolution is defined as $d_{lat}^2 d_{ax}$, where d_{lat} is the sampling-limited lateral FWHM size and d_{ax} is the sampling-limited axial FWHM size of the point spread function. Lateral sampling can be adjusted by changing the magnification of the detection system, which typically affects both volume throughput and effective resolution (for examples, see ×1.26 versus ×12.6 magnification settings for the LaVision BioTec ultramicroscope or ×16 versus ×32 magnification settings for IsoView). Data points for custom light-sheet and two-photon microscopy refer to imaging of hippocampal dendrites[14], *Caenorhabditis elegans* development[111], cellular dynamics[110], zebrafish nervous system[105,112] and mouse brains[54]. Data points for commercial microscopes reflect the technical specifications provided by the manufacturer[165,166]. All techniques included in the plot have been successfully applied to the imaging of cleared tissues. **c** | Working distance of the detection systems for the methods shown in parts **a** and **b**. The design by Economo et al.[54] does not require long-working-distance optics for imaging mouse brains since their microscope is integrated with a tissue vibratome. Chhetri et al.[112] surrounded the specimen with four identical objectives for illumination and fluorescence detection, which allows an increase in the bidirectional working distance by a factor of 2 (compared with the native working distance of a single objective) in the special case of imaging transparent, cleared tissues. The maximum supported specimen size can in principle also be doubled in other light-sheet techniques at the expense of temporal resolution by rotating the specimen by 180° and acquiring volumetric data from this opposite view. Tomer et al.[105] proposed using the majority of the detection objective's working distance to introduce a block of high-refractive-index material in the detection path. The effective working distance (distance between the block and the in-focus region of the specimen) is thus typically not identical to the native working distance of the objective. For this reason, the latter technique is not included in this plot.

and allow the illumination of exceptionally thin sections of a specimen (FIG. 5). Moreover, high resolution on the order of 300–400 nm in all spatial directions has also been realized by combining light-sheet microscopy with the concept of multiview imaging[111–113]. The key idea behind this latter approach is that the directions along which resolution is low and high, respectively, can be permuted by imaging the same specimen twice from two orthogonal views. When the complementary information from these views is combined by image processing, the low axial resolution observed in one given view of the specimen can thus simply be replaced by the much greater lateral resolution offered by the second, perpendicular view of the same specimen. This concept of multiview imaging, as it has been implemented in diSPIM[111] and IsoView[112] light-sheet microscopy, is a particularly

promising candidate for high-resolution imaging of large volumes, since it can be implemented in a way that offers high spatial resolution over a large field of view at exceptionally high volume acquisition rates[112]. For example, in IsoView microscopy, this concept allows an isotropic spatial resolution of 400 nm at a volume throughput of more than $10^8 \mu m^3$ per second, while offering the long working distance needed for imaging large specimens without physical sectioning (FIG. 5). Irrespective of the choice of microscope implementation, the imaging of large samples furthermore benefits from automation strategies and computational techniques for adapting the microscope to the specimen's optical properties. Although cleared specimens are exceptionally transparent, remaining spatial variability in the RI or small mismatches in the RIs of the specimen and the imaging medium can perturb the light path both in light-sheet illumination and in fluorescence detection. To ensure optimal overlap between light sheets and detection focal planes throughout the specimen volume — and thus optimal resolution, contrast and signal strength — adaptive imaging and autofocusing techniques have been developed[104,114–116], which are conceptually compatible with most existing light-sheet microscope designs.

When one is imaging very large specimens in the millimetre or even centimetre range, it is important to note that even techniques with a relatively large field of view typically cannot fit the entire specimen within their native imaging volume. These limitations arise from a fundamental trade-off between field size and numerical aperture (and thus resolution) in the design of conventional optics, constraints related to the properties of high-end digital cameras, and from challenges associated with the creation of sufficiently thin light sheets over a large field of view. Thus, a typical workaround in existing approaches to high-resolution imaging of large samples, such as lattice light-sheet microscopy or IsoView light-sheet microscopy, is to rely on tiling strategies for imaging specimens as large as entire cleared and/or expanded nervous systems[117,118]. This approach largely decouples specimen size from spatial resolution, allowing state-of-the-art microscopes to produce images of optimal quality irrespective of whether the instrument is used to image single cells or an entire brain (assuming good performance of the tissue-clearing method). The two downsides of this approach are the limited data throughout, owing to the sequential nature of optical tiling, and the need for sophisticated computational methods for image processing (see the next section). Ongoing research efforts are therefore investigating other possible solutions to these bottlenecks, including the development of axially swept light-sheet microscopy[119] and alternative optical strategies for generating light sheets[120].

In the future, we expect to see powerful, new implementations of light-sheet microscopy that combine these latest breakthroughs in high-speed, high-resolution imaging with new large-aperture, long-working-distance detection optics developed by several major optics companies specifically for imaging large cleared tissues. Moreover, further advances in imaging speed will become possible by pursuing multiplexing strategies that parallelize the imaging process across large tissue volumes.

Data analysis and management

With the advent of powerful microscopes that allow high-speed, high-resolution imaging of large specimens, there is a need for new computational approaches that tackle downstream challenges in large-scale data analysis and management. For example, a raw recording of a single mouse brain obtained with high-resolution light microscopy typically comprises thousands of individual 3D subvolumes (also referred to as 'tiles') and tens of terabytes of image data. The tiling of image acquisition is usually necessary owing to the limited field of view of light microscopes, which, for specimens as large as a mouse brain, can capture only a small portion of the specimen volume at a time. Thus, translation of either specimen or optics and sequential acquisition of multiple subvolumes is required to eventually arrive at an image of the entire specimen. To efficiently store, process and extract biological meaning from the resulting image data, powerful computational methods are needed to facilitate the following: large-scale data management; multitile image registration and fusion; image analysis and mapping of image data to existing brain atlases; and visualization and interactive viewing of the 3D image data. Each of these challenges is the focus of ongoing efforts in the field, and a range of useful computational tools are now available.

In the realm of data management, recent efforts have led to the creation of several file formats designed to facilitate rapid compression and decompression of large-scale light microscopy image data. The KLB file format is a block-based, lossless compression format that provides JPEG2000-like compression factors while increasing write and read speeds fivefold (up to 500 and 1,000 MB per second, respectively)[121]. The block-based implementation furthermore offers fast access to local regions in large multidimensional images. KLB supports integration of other compression algorithms in the block-based container and requires only a CPU, thus allowing effective deployment on inexpensive, lower-end computers. By combining KLB with background masking, a 30-fold to 500-fold reduction in data size was achieved[121]. Similarly, the BigDataViewer[122] Fiji plugin leverages the infrastructure of the ImageJ ecosystem[123], namely the ImgLib2 library[124], to provide seamless access to various block-based data formats, including KLB, hierarchical data format version 5 (HDF5), Imaris and CATMAID (collaborative annotation toolkit for massive amounts of image data). In addition, it provides a powerful caching scheme that ensures that data are transferred optimally. When coupled with the HDF5 container, for example, in the context of multiview reconstructions of light-sheet microscopy data[125,126], BigDataViewer allows straightforward combination with arbitrary compression schemes. The reliance on ImgLib2, which is designed to write efficient image analysis algorithms in Java independent of the data type (8-bit, 16-bit, RGB and so on), dimensionality (1D to nD) and storage strategy (memory, local or remote file systems), makes it possible to deploy through BigDataViewer complex image processing pipelines on virtually limitless data. The B³D format offers a complementary approach to high-performance data compression using graphics processing unit-based compute unified device architecture

---

Hierarchical data format version 5
(HDF5). A hierarchical data format and versatile data model to manage and represent extremely large and complex data objects.

Compute unified device architecture
(CUDA). A parallel computing platform and programming model developed by Nvidia for general computing on its own graphics processing units.

(CUDA) processing[127]. Although B³D does not use a block-based architecture, it offers excellent write/read speeds on the order of 1,000 MB per second and includes lossless and lossy compression schemes. A reduction in storage requirements and a speed-up of computational processing of image data can also be achieved by using alternative representations of the information encoded in an image. For example, the adaptive particle representation adaptively resamples an image, guided by local information content and using local gain control, and stores the information as a set of particle cells with associated intensity values[128]. The developers of the adaptive particle representation showed that such a representation not only facilitates data compaction but also has the potential to speed up subsequent image processing steps, such as filtering or image segmentation. The challenge will be to adapt existing image processing solutions to this new data representation paradigm.

Transforming the raw image data of a large, cleared specimen into a spatially coherent, high-resolution image volume that is suitable for data visualization and analysis involves several critical steps. The individual image tiles need to be precisely aligned and fused, and an additional multiview deconvolution step may be needed if complementary views of the specimen were recorded with the light microscope. BigStitcher is scalable and efficient software that facilitates such computations for terabyte-scale image data of large specimens, such as entire mammalian brains or entire invertebrate nervous systems[117]. This tool leverages the power of ImgLib2 and BigDataViewer and is conveniently available as a plugin for the widely used image processing package Fiji[129]. Once these initial image processing steps are complete and a high-quality image volume of the complete specimen has been reconstructed, downstream analyses and data mining frequently involve mapping and comparison of the image data with an anatomical reference atlas, image segmentation, annotation of the image data, and interactive data visualization. For the mapping of image volumes to each other or to a common anatomical atlas, several tools have been developed[130–132], but they currently cannot process very large data volumes. Bigwarp[133] allows manual, interactive, landmark-based deformable image alignment on arbitrarily large images as it uses BigDataViewer for visualization and navigation and a thin plate spline implemented in Java to build a deformation from point correspondences[134]. For image segmentation, powerful approaches to image analysis based on machine learning are quickly gaining momentum. The iLastik toolkit has been widely adopted as a user-friendly framework for interactive image classification and segmentation with an intuitive graphical user interface[135]. Familiarity with machine learning algorithms or expertise in image processing is not required to use this toolkit, as the user communicates with the software simply by labelling a small subset of the image data, thus visually indicating the desired classification scheme. iLastik then learns from these user-provided labels to build classifiers that are suitable for automated processing of large data sets. Real-time feedback furthermore allows the user to iteratively refine segmentation results and update the respective classifiers.

Other software tools support the investigation of structure–function relationships in the mouse brain. For example, an open-source framework consisting of the software packages WholeBrain and OpenBrainMap[136] allows integration of anatomical, molecular and functional light-microscopy image data. This framework uses information and definitions from the mouse reference atlas generated by the Allen Institute[137,138], and it includes tools for mapping labelled neurons into a versatile, standardized brain atlas, statistical data analysis and visualization and sharing of data through an interactive Web interface. CATMAID[139] is another useful software framework that provides efficient access to large-scale electron and light microscopy image data sets as well as an infrastructure for collaborative annotation of such data through a decentralized Web interface. These design principles have been enabling not only for applications in neuroscience, and the field of connectomics in particular[140], but also for large-scale projects in other areas of the life sciences, such as whole-tissue cell tracking in developmental biology[141]. Finally, powerful methods designed to specifically address the need for interactive 3D visualization of large images contribute another essential facet to the spectrum of open-source tools for handling high-resolution images of large, cleared specimens. BigDataViewer[122] and TeraFly[142] allow 3D viewing of large image stacks and are designed to be very responsive to user manipulation of the specimen's coordinate system, such as translation, rotation and zoom. BigDataViewer is smoothly integrated in the Fiji ecosystem and plays a central role in advanced software suites such as BigStitcher, BigWarp and MaMuT for manual segmentation and tracking of cells in multiview light-sheet microscopy data[143]. TeraFly is designed in a particularly memory-efficient way and provides true 3D rendering capabilities, such as real-time alpha blending, as well as a 'Virtual Finger' feature that maps user input from the 2D plane of the computer screen to the 3D location in the data set corresponding to the selected biological structure.

Future objectives

Classical histology is typically performed on only a few selected thin slices. However, analysis of selected tissue sections is prone to inevitable biases because one may miss important biomedical information that is located elsewhere. By contrast, 3D histology on intact transparent specimens provides a much greater amount of information and thus a greater level of insight into anatomy and pathology. Moreover, it can speed up and reduce the cost of histology by several-thousand-fold compared with classical histology approaches.

Although the efficacy of tissue-clearing methods has improved considerably, we still lack a rigorous understanding of the physical and chemical principles underlying tissue-clearing processes. Moreover, we still need more robust labelling, imaging and data analysis tools to broaden the applications of tissue-clearing methods. In particular, we need the following: rapid and homogeneous protein and RNA labelling methods for whole organs of rodents and primates, large human tissues and, even, whole adult rodent and primate bodies; light-sheet microscopes that are capable of imaging tissues as large

as organs and bodies of adult rodents and primates with isotropic subcellular resolution (less than 1 μm); and faster and more accurate algorithms for stitching, atlas registration and structure recognition in data sets larger than tens of terabytes. Furthermore, a standard atlas of organs and bodies of rodent and primates is required to quantitatively compare protein and RNA expression in different individuals. It would be ideal if new methods such as multiplexed robust fluorescence in situ hybridization, which allows imaging of dozens of mRNAs on brain sections, could also be combined with tissue-clearing methods[144]. We also expect that tissue-clearing methods will be combined with other prominent technologies, including single-cell RNA sequencing and mass spectrometry, to obtain spatial and temporal information on the quality and quantity of RNAs and proteins over entire organs and bodies.

In the future, tissue-clearing methods will significantly impact the drug development process by introducing unbiased readouts of entire organs and bodies in treated versus control groups, thereby assessing whether drug candidates for given neurological diseases can cross the blood–brain barrier and whether they can bind to desired targets in the brain and spinal cord at the level of single cells. Until now, targeting the amyloid peptides in the plaques by specific antibodies has been a major endeavour in an effort to develop an effective treatment for Alzheimer disease, but clinical trials of this approach have failed to show any efficacy. We speculate that one of the major contributing reasons for the failure in translational research is the lack of technologies that truly assess the targeting of such drugs at single-cell resolution in the whole body of preclinical animal models. Therefore, monitoring biodistributions and actions of drugs at single-cell resolution will be critical to comprehensively understand underlying cellular mechanisms and thereby design effective drugs. In this regard, nanotechnology will also greatly facilitate targeted drug delivery in many fields of biomedical science, including neuroscience. The effects of nanoparticle-based drugs are currently assessed by coarse imaging methods such as bioluminescence, which can detect the signal only when they are of millimetre size, significantly jeopardizing the use of nanoparticles to conduct nanoscale functions. Tissue-clearing methods will be a key technology in the development of drug-carrying nanoparticles, as such methods will allow identification of these agents in the whole rodent and primate bodies at single-cell resolution.

3D histopathology provided by tissue-clearing methods will also significantly scale up the investigation of human tissues in both preclinical and clinical arenas. For example, labelling and imaging whole human biopsy samples from patients with cancer (several thousand times larger than in classical histology) at single-cell resolution will provide much faster and more accurate diagnosis and staging of the tumours. Finally, clearing, labelling and imaging of adult human tissues on the order of centimetres will be one of the primary technologies to reveal the cellular structure of whole organs and eventually map circuits in whole human brains.

Published online: 02 January 2020

1. Spalteholz, W. *Über das Durchsichtigmachen von Menschlichen und Tierischen Präparaten*. (S. Hirzel, 1914).
2. Chung, K. et al. Structural and molecular interrogation of intact biological systems. *Nature* **497**, 332–337 (2013).
   This article is the first to demonstrate in situ synthesis of a hydrogel and its fusion with tissue via covalent bonds to form a tissue–hydrogel hybrid.
3. Yang, B. et al. Single-cell phenotyping within transparent intact tissue through whole-body clearing. *Cell* **158**, 945–958 (2014).
   This article first reports clearing of adult rodents via the vasculature; RNA detection in cleared tissues with single-molecule resolution by single-molecule fluorescence in situ hybridization and that specific formulations of tissue–hydrogel hybrids can significantly expand.
4. Renier, N. et al. iDISCO: a simple, rapid method to immunolabel large tissue samples for volume imaging. *Cell* **159**, 896–910 (2014).
5. Susaki, E. A. et al. Whole-brain imaging with single-cell resolution using chemical cocktails and computational analysis. *Cell* **157**, 726–739 (2014).
   This article first reports on the delipidation activity of amino alcohols and the high-performance hydrophilic tissue-clearing method CUBIC and reports tissue clearing of the marmoset brain.
6. Tainaka, K. et al. Whole-body imaging with single-cell resolution by tissue decolorization. *Cell* **159**, 911–924 (2014).
   This article first demonstrates that decolourization of haem is possible in mild chemical conditions by amino alcohols, and reports whole-body imaging of the adult mouse.
7. Ertürk, A. et al. Three-dimensional imaging of the unsectioned adult spinal cord to assess axon regeneration and glial responses after injury. *Nat. Med.* **18**, 166–171 (2012).
   This work demonstrates the application of an organic solvent-clearing method (3DISCO) on the intact adult mouse CNS to study neurodegeneration and regeneration.
8. Belle, M. et al. A simple method for 3D analysis of immunolabeled axonal tracts in a transparent nervous system. *Cell Rep.* **9**, 1191–1201 (2014).
   This work is the first to combine whole-mount immunostaining, 3DISCO clearing and light-sheet microscopy to analyse axon guidance defects in mutant mice.
9. Treweek, J. B. et al. Whole-body tissue stabilization and selective extractions via tissue-hydrogel hybrids for high-resolution intact circuit mapping and phenotyping. *Nat. Protoc.* **10**, 1860–1896 (2015).
10. Costantini, I. et al. A versatile clearing agent for multi-modal brain imaging. *Sci. Rep.* **5**, 9808 (2015).
11. Klingberg, A. et al. Fully automated evaluation of total glomerular number and capillary tuft size in nephritic kidneys using lightsheet microscopy. *J. Am. Soc. Nephrol.* **28**, 452–459 (2017).
12. Hama, H. et al. Scale: a chemical approach for fluorescence imaging and reconstruction of transparent mouse brain. *Nat. Neurosci.* **14**, 1481–1488 (2011).
13. Ke, M.-T., Fujimoto, S. & Imai, T. SeeDB: a simple and morphology-preserving optical clearing agent for neuronal circuit reconstruction. *Nat. Neurosci.* **16**, 1154–1161 (2013).
14. Dodt, H. U. et al. Ultramicroscopy: three-dimensional visualization of neuronal networks in the whole mouse brain. *Nat. Methods* **4**, 331–336 (2007).
15. Susaki, E. A. & Ueda, H. R. Whole-body and whole-organ clearing and imaging techniques with single-cell resolution: toward organism-level systems biology in mammals. *Cell Chem. Biol.* **23**, 137–157 (2016).
16. Tainaka, K., Kuno, A., Kubota, S. I., Murakami, T. & Ueda, H. R. Chemical principles in tissue clearing and staining protocols for whole-body cell profiling. *Annu. Rev. Cell Dev. Biol.* **32**, 713–741 (2016).
17. Murakami, T. C. et al. A three-dimensional single-cell-resolution whole-brain atlas using CUBIC-X expansion microscopy and tissue clearing. *Nat. Neurosci.* **21**, 625–637 (2018).
   This article first demonstrates the polymer-gel property of a fixed mouse brain in the absence of exogenous polymers, reports expansion microscopy using hydrophilic reagents and reports the generation of a 3D single-cell-resolution mouse brain atlas, the CUBIC-Atlas.
18. Amiya, T. & Tanaka, T. Phase transitions in crosslinked gels of natural polymers. *Macromolecules* **20**, 1162–1164 (1987).
19. Shibayama, M. & Tanaka, T. in *Responsive Gels: Volume Transitions I* 1–62 (Springer, 1993).
20. Lorentz, H. A. Ueber die Beziehung zwischen der Fortpflanzungsgeschwindigkeit des Lichtes und der Körperdichte. *Ann. Phys.* **9**, 641–665 (1880).
21. Lorenz, L. Ueber die Refractionsconstante. *Ann. Phys.* **11**, 70–103 (1880).
22. Tainaka, K. et al. Chemical landscape for tissue clearing based on hydrophilic reagents. *Cell Rep.* **24**, 2196–2210 (2018).
   This article first reports the chemical profiling of hydrophilic tissue-clearing reagents and proposes chemical principles of hydrophilic tissue-clearing methods.
23. Belle, M. et al. Tridimensional visualization and analysis of early human development. *Cell* **169**, 161–173 e112 (2017).
   This study uses 3D imaging of cleared human embryos and fetuses to provide the first comprehensive description of the development of the human peripheral nervous system and the innervation pattern of many organs in intact specimens.
24. Kim, S. Y. et al. Stochastic electrotransport selectively enhances the transport of highly electromobile molecules. *Proc. Natl Acad. Sci. USA* **112**, E6274–E6283 (2015).
25. Murray, E. et al. Simple, scalable proteomic imaging for high-dimensional profiling of intact systems. *Cell* **163**, 1500–1514 (2015).
   This article is the first to demonstrate that controlling the chemical interaction time and kinetics achieves more uniform and scalable processing of large-scale tissues.
26. Renier, N. et al. Mapping of brain activity by automated volume analysis of immediate early genes. *Cell* **165**, 1789–1802 (2016).

27. Kubota, S. I. et al. Whole-body profiling of cancer metastasis with single-cell resolution. *Cell Rep.* **20**, 236–250 (2017).

28. Cai, R. et al. Panoptic imaging of transparent mice reveals whole-body neuronal projections and skull–meninges connections. *Nat. Neurosci.* **22**, 317–327 (2019).
This study shows that vDISCO boosted fluorescent protein signal in intact transparent mice, thereby allowing detection of widespread CNS trauma effects, and reveals short vascular connections between the skull marrow and brain meninges.

29. Deverman, B. E. et al. Cre-dependent selection yields AAV variants for widespread gene transfer to the adult brain. *Nat. Biotechnol.* **34**, 204–209 (2016).
This is the first article to report efficient crossing of the blood–brain barrier in adult rodents by an engineered adeno-associated virus vector able to package the cargo of choice. A Cre-enzyme-based viral-vector screening method is introduced and it is demonstrated how whole-body tissue clearing can facilitate transduction maps of systemically delivered genes.

30. Bedbrook, C. N., Deverman, B. E. & Gradinaru, V. Viral strategies for targeting the central and peripheral nervous systems. *Annu. Rev. Neurosci.* **41**, 323–348 (2018).

31. Keller, P. J. & Ahrens, M. B. Visualizing whole-brain activity and development at the single-cell level using light-sheet microscopy. *Neuron* **85**, 462–483 (2015).

32. Vigouroux, R. J., Belle, M. & Chêdotal, A. Neuroscience in the third dimension: shedding new light on the brain with tissue clearing. *Mol. Brain* **10**, 33 (2017).

33. Ertürk, A. et al. Three-dimensional imaging of solvent-cleared organs using 3DISCO. *Nat. Protoc.* **7**, 1983–1995 (2012).

34. Liu, Z. et al. Immune homeostasis enforced by co-localized effector and regulatory T cells. *Nature* **528**, 225–230 (2015).

35. Acar, M. et al. Deep imaging of bone marrow shows non-dividing stem cells are mainly perisinusoidal. *Nature* **526**, 126–130 (2015).

36. Espinosa-Medina, I. et al. Parasympathetic ganglia derive from Schwann cell precursors. *Science* **345**, 87–90 (2014).

37. Oshimori, N., Oristian, D. & Fuchs, E. TGF-β promotes heterogeneity and drug resistance in squamous cell carcinoma. *Cell* **160**, 963–976 (2015).

38. Garofalo, S. et al. Enriched environment reduces glioma growth through immune and non-immune mechanisms in mice. *Nat. Commun.* **6**, 6623 (2015).

39. von Neubeck, B. et al. An inhibitory antibody targeting carbonic anhydrase XII abrogates chemoresistance and significantly reduces lung metastases in an orthotopic breast cancer model in vivo. *Int. J. Cancer* **143**, 2065–2075 (2018).

40. Tanaka, N. et al. Whole-tissue biopsy phenotyping of three-dimensional tumours reveals patterns of cancer heterogeneity. *Nat. Biomed. Eng.* **1**, 796–806 (2017).

41. Garvalov, B. K. & Ertürk, A. Seeing whole-tumour heterogeneity. *Nat. Biomed. Eng.* **1**, 772–774 (2017).

42. Pan, C. et al. Shrinkage-mediated imaging of entire organs and organisms using uDISCO. *Nat. Methods* **13**, 859–867 (2016).

43. Herisson, F. et al. Direct vascular channels connect skull bone marrow and the brain surface enabling myeloid cell migration. *Nat. Neurosci.* **21**, 1209–1217 (2018).

44. Pan, C. et al. Deep learning reveals cancer metastasis and therapeutic antibody targeting in whole body. *Cell* **179**, 1661–1676.e19 (2019).
This works describes a novel method to detect and quantify cancer metastasis and antibody drug targeting at cellular resolution in the entire mouse using whole-body tissue clearing and deep learning.

45. Chiang, A. S. et al. Three-dimensional mapping of brain neuropils in the cockroach, Diploptera punctata. *J. Comp. Neurol.* **440**, 1–11 (2001).

46. Liu, Y.-C. & Chiang, A.-S. High-resolution confocal imaging and three-dimensional rendering. *Methods* **30**, 86–93 (2003).

47. Richardson, D. S. & Lichtman, J. W. Clarifying Tissue Clearing. *Cell* **162**, 246–257 (2015).

48. Hirshburg, J., Choi, B., Nelson, J. S. & Yeh, A. T. Correlation between collagen solubility and skin optical clearing using sugars. *Lasers Surg. Med.* **39**, 140–144 (2007).

49. Hama, H. et al. ScaleS: an optical clearing palette for biological imaging. *Nat. Neurosci.* **18**, 1518–1529 (2015).

50. Chance, B., Liu, H., Kitai, T. & Zhang, Y. Effects of solutes on optical properties of biological materials: models, cells, and tissues. *Anal. Biochem.* **227**, 351–362 (1995).

51. Ke, M.-T. et al. Super-resolution mapping of neuronal circuitry with an index-optimized clearing agent. *Cell Rep.* **14**, 2718–2732 (2016).

52. Susaki, E. A. et al. Advanced CUBIC protocols for whole-brain and whole-body clearing and imaging. *Nat. Protoc.* **10**, 1709–1727 (2015).

53. Tatsuki, F. et al. Involvement of Ca²⁺-dependent hyperpolarization in sleep duration in mammals. *Neuron* **90**, 70–85 (2016).

54. Economo, M. N. et al. A platform for brain-wide imaging and reconstruction of individual neurons. *eLife* **5**, e10566 (2016).

55. Wang, L. et al. The coding of valence and identity in the mammalian taste system. *Nature* **558**, 127–131 (2018).

56. Justus, D. et al. Glutamatergic synaptic integration of locomotion speed via septoentorhinal projections. *Nat. Neurosci.* **20**, 16–19 (2017).

57. Romanov, R. A. et al. Molecular interrogation of hypothalamic organization reveals distinct dopamine neuronal subtypes. *Nat. Neurosci.* **20**, 176–188 (2017).

58. Lanjakornsiripan, D. et al. Layer-specific morphological and molecular differences in neocortical astrocytes and their dependence on neuronal layers. *Nat. Commun.* **9**, 1623 (2018).

59. Rousso, D. L. et al. Two pairs of on and off retinal ganglion cells are defined by intersectional patterns of transcription factor expression. *Cell Rep.* **15**, 1930–1944 (2016).

60. Chen, J. Y. et al. Hoxb5 marks long-term haematopoietic stem cells and reveals a homogenous perivascular niche. *Nature* **530**, 223–227 (2016).

61. Cuccarese, M. F. et al. Heterogeneity of macrophage infiltration and therapeutic response in lung carcinoma revealed by 3D organ imaging. *Nat. Commun.* **8**, 14293 (2017).

62. Davis, F. M. et al. Single-cell lineage tracing in the mammary gland reveals stochastic clonal dispersion of stem/progenitor cell progeny. *Nat. Commun.* **7**, 13053 (2016).

63. Li, J. et al. Single-cell lineage tracing reveals that oriented cell division contributes to trabecular morphogenesis and regional specification. *Cell Rep.* **15**, 158–170 (2016).

64. Yamamoto, J. et al. Neuronal signals regulate obesity induced beta-cell proliferation by FoxM1 dependent mechanism. *Nat. Commun.* **8**, 1930 (2017).

65. Chen, F., Tillberg, P. W. & Boyden, E. S. Expansion microscopy. *Science* **347**, 543–548 (2015).
This article first reports the concept of expansion microscopy based on an exogenous hydrogel polymer.

66. Matsumoto, K. *et al.* Advanced CUBIC tissue clearing for whole-organ cell profiling. *Nat. Protoc.* **14**, 3506–3537 (2019).

67. Tomer, R., Ye, L., Hsueh, B. & Deisseroth, K. Advanced CLARITY for rapid and high-resolution imaging of intact tissues. *Nat. Protoc.* **9**, 1682–1697 (2014).

68. Gradinaru, V., Treweek, J., Overton, K. & Deisseroth, K. Hydrogel-tissue chemistry: principles and applications. *Annu. Rev. Biophys.* **47**, 355–376 (2018).

69. Ku, T. et al. Multiplexed and scalable super-resolution imaging of three-dimensional protein localization in size-adjustable tissues. *Nat. Biotechnol.* **34**, 973–981 (2016).

70. Sylwestrak, E. L., Rajasethupathy, P., Wright, M. A., Jaffe, A. & Deisseroth, K. Multiplexed intact-tissue transcriptional analysis at cellular resolution. *Cell* **164**, 792–804 (2016).

71. Park, Y.-G. et al. Protection of tissue physicochemical properties using polyfunctional crosslinkers. *Nat. Biotechnol.* **37**, 73–83 (2019).
This article is the first to demonstrate protection of tissue and biomolecular properties against harsh stress using polyfunctional crosslinkers.

72. Renner, M. et al. Self-organized developmental patterning and differentiation in cerebral organoids. *EMBO J.* **36**, 1316–1329 (2017).

73. Canter, R. G. et al. 3D mapping reveals network-specific amyloid progression and subcortical susceptibility in mice. *Commun. Biol.* **2**, 360 (2019).

74. Greenbaum, A. et al. Bone CLARITY: clearing, imaging, and computational analysis of osteoprogenitors within intact bone marrow. *Sci. Transl Med.* **9**, eaah6518 (2017).
This article reports clearing of whole bone with preserved marrow and imaging endogenous fluorescence with single-cell resolution throughout the marrow by light-sheet microscopy.

75. Greenbaum, A., Jang, M. J., Challis, C. & Gradinaru, V. Q&A: how can advances in tissue clearing and optogenetics contribute to our understanding of normal and diseased biology? *BMC Biol.* **15**, 87 (2017).

76. Shah, S. et al. Single-molecule RNA detection at depth via hybridization chain reaction and tissue hydrogel embedding and clearing. *Development* **143**, 2862–2867 (2016).

77. DePas, W. H. et al. Exposing the three-dimensional biogeography and metabolic states of pathogens in cystic fibrosis sputum via hydrogel embedding, clearing, and rRNA labeling. *mBio* **7**, e00796–e00816 (2016).

78. Treweek, J. B. & Gradinaru, V. Extracting structural and functional features of widely distributed biological circuits with single cell resolution via tissue clearing and delivery vectors. *Curr. Opin. Biotechnol.* **40**, 193–207 (2016).

79. Menegas, W. et al. Dopamine neurons projecting to the posterior striatum form an anatomically distinct subclass. *eLife* **4**, e10032 (2015).

80. Chan, K. Y. et al. Engineered AAVs for efficient noninvasive gene delivery to the central and peripheral nervous systems. *Nat. Neurosci.* **20**, 1172–1179 (2017).
This article reports novel viral vectors to deliver cargo to neurons throughout the brain and body via the bloodstream, and a complementary vector toolbox for sparse stochastic labelling for morphological assessment. These delivery methods for Golgi-like genetic labelling can complement tissue clearing and microscopy methods to yield refined maps of the nervous system across the brain and body.

81. Robinson, J. E. & Gradinaru, V. Dopaminergic dysfunction in neurodevelopmental disorders: recent advances and synergistic technologies to aid basic research. *Curr. Opin. Neurobiol.* **48**, 17–29 (2018).

82. Liebmann, T. et al. Three-dimensional study of Alzheimer's disease hallmarks using the iDISCO clearing method. *Cell Rep.* **16**, 1138–1152 (2016).

83. Welniarz, Q. et al. Non cell-autonomous role of DCC in the guidance of the corticospinal tract at the midline. *Sci. Rep.* **7**, 410 (2017).

84. Hruska, M., Henderson, N., Le Marchand, S. J., Jafri, H. & Dalva, M. B. Synaptic nanomodules underlie the organization and plasticity of spine synapses. *Nat. Neurosci.* **21**, 671–682 (2018).

85. Ando, K. et al. Inside Alzheimer brain with CLARITY: senile plaques, neurofibrillary tangles and axons in 3-D. *Acta Neuropathol.* **128**, 457–459 (2014).

86. Morawski, M. et al. Developing 3D microscopy with CLARITY on human brain tissue: towards a tool for informing and validating MRI-based histology. *Neuroimage* **182**, 417–428 (2018).

87. Phillips, J. et al. Development of passive CLARITY and immunofluorescent labelling of multiple proteins in human cerebellum: understanding mechanisms of neurodegeneration in mitochondrial disease. *Sci. Rep.* **6**, 26013 (2016).

88. Liu, A. K. L. et al. Bringing CLARITY to the human brain: visualization of Lewy pathology in three dimensions. *Neuropathol. Appl. Neurobiol.* **42**, 573–587 (2016).

89. Lee, E. et al. ACT-PRESTO: rapid and consistent tissue clearing and labeling method for 3-dimensional (3D) imaging. *Sci. Rep.* **6**, 18631 (2016).

90. Lai, H. M. et al. Next generation histology methods for three-dimensional imaging of fresh and archival human brain tissues. *Nat. Commun.* **9**, 1066 (2018).

91. Allen, J. S., Damasio, H. & Grabowski, T. J. Normal neuroanatomical variation in the human brain: an MRI-volumetric study. *Am. J. Phys. Anthropol.* **118**, 341–358 (2002).

92. Birey, F. et al. Assembly of functionally integrated human forebrain spheroids. *Nature* **545**, 54–59 (2017).

93. Casoni, F. et al. Development of the neurons controlling fertility in humans: new insights from 3D imaging and transparent fetal brains. *Development* **143**, 3969–3981 (2016).

94. Hsueh, B. et al. Pathways to clinical CLARITY: volumetric analysis of irregular, soft, and heterogeneous tissues in development and disease. *Sci. Rep.* **7**, 5899 (2017).

95. Behjati, S., Lindsay, S., Teichmann, S. A. & Haniffa, M. Mapping human development at single-cell resolution. *Development* **145**, dev152561 (2018).

96. Kieffer, C., Ladinsky, M. S., Ninh, A., Galimidi, R. P. & Bjorkman, P. J. Longitudinal imaging of HIV-1 spread in humanized mice with parallel 3D immunofluorescence and electron tomography. *eLife* **6**, e23282 (2017).

REVIEWS

97. Dantzer, R., O'Connor, J. C., Freund, G. G., Johnson, R. W. & Kelley, K. W. From inflammation to sickness and depression: when the immune system subjugates the brain. *Nat. Rev. Neurosci.* **9**, 46–56 (2008).

98. Glaser, A. K. et al. Light-sheet microscopy for slide-free non-destructive pathology of large clinical specimens. *Nat. Biomed. Eng.* **1**, 0084 (2017).

99. Nojima, S. et al. CUBIC pathology: three-dimensional imaging for pathological diagnosis. *Sci. Rep.* **7**, 9269 (2017).

100. Royen, M. E. et al. Three-dimensional microscopic analysis of clinical prostate specimens. *Histopathology* **69**, 985–992 (2016).

101. Huisken, J., Swoger, J., Del Bene, F., Wittbrodt, J. & Stelzer, E. H. Optical sectioning deep inside live embryos by selective plane illumination microscopy. *Science* **305**, 1007–1009 (2004).

102. Keller, P. J., Schmidt, A. D., Wittbrodt, J. & Stelzer, E. H. K. Reconstruction of zebrafish early embryonic development by scanned light sheet microscopy. *Science* **322**, 1065–1069 (2008).

103. Voie, A. H., Burns, D. H. & Spelman, F. A. Orthogonal-plane fluorescence optical sectioning: three-dimensional imaging of macroscopic biological specimens. *J. Microsc.* **170**, 229–236 (1993).

104. Ryan, D. P. et al. Automatic and adaptive heterogeneous refractive index compensation for light-sheet microscopy. *Nat. Commun.* **8**, 612 (2017).

105. Tomer, R. et al. SPED light sheet microscopy: fast mapping of biological system structure and function. *Cell* **163**, 1796–1806 (2015).

106. Gómez-Gaviro, M. V. et al. Optimized CUBIC protocol for 3D imaging of chicken embryos at single-cell resolution. *Development* **44**, 2092–2097 (2017).

107. Stefaniuk, M. et al. Light-sheet microscopy imaging of a whole cleared rat brain with Thy1-GFP transgene. *Sci. Rep.* **6**, 28209 (2016).

108. Niedworok, C. J. et al. Charting monosynaptic connectivity maps by two-color light-sheet fluorescence microscopy. *Cell Rep.* **2**, 1375–1386 (2012).

109. Planchon, T. A. et al. Rapid three-dimensional isotropic imaging of living cells using Bessel beam plane illumination. *Nat. Methods* **8**, 417–423 (2011).

110. Chen, B. C. et al. Lattice light-sheet microscopy: imaging molecules to embryos at high spatiotemporal resolution. *Science* **346**, 1257998 (2014).
This article describes lattice light-sheet microscopy, which uses very thin laser light sheets for fluorescence generation and introduces a light-efficient concept for high-resolution imaging of a field of view of approximately 100 μm.

111. Wu, Y. C. et al. Spatially isotropic four-dimensional imaging with dual-view plane illumination microscopy. *Nat. Biotechnol.* **31**, 1032–1038 (2013).
This article describes diSPIM light-sheet microscopy, which rapidly acquires two orthogonal views of a specimen with a field of view of several hundred micrometres and hence combines high imaging speeds with a high, spatially isotropic resolution of 330 nm.

112. Chhetri, R. K. et al. Whole-animal functional and developmental imaging with isotropic spatial resolution. *Nat. Methods* **12**, 1171–1178 (2015).
By allowing simultaneous orthogonal four-view imaging with a field of view approaching a 1 mm, IsoView light-sheet microscopy achieves a volume throughput of more than 10^8 μm³ per second and a high, spatially isotropic resolution of 400 nm.

113. Swoger, J., Verveer, P., Greger, K., Huisken, J. & Stelzer, E. H. Multi-view image fusion improves resolution in three-dimensional microscopy. *Opt. Express* **15**, 8029–8042 (2007).

114. Royer, L. A. et al. Adaptive light-sheet microscopy for long-term, high-resolution imaging in living organisms. *Nat. Biotechnol.* **34**, 1267–1278 (2016).

115. Royer, L. A., Lemon, W. C., Chhetri, R. K. & Keller, P. J. A practical guide to adaptive light-sheet microscopy. *Nat. Protoc.* **13**, 2462–2500 (2018).

116. Silvestri, L. et al. RAPID: real-time image-based autofocus for all wide-field optical microscopy systems. Preprint at *bioRxiv* https://doi.org/10.1101/170555 (2017).

117. Hörl, D. et al. BigStitcher: reconstructing high-resolution image datasets of cleared and expanded samples. *Nat. Methods* **16**, 870–874 (2019).
This artcle describes BigStitcher, which offers highly customizable stitching of arbitrarily large image mosaics and multiview selective plane illumination microscopy data building on the BigDataViewer infrastructure in Fiji.

118. Gao, R. et al. Cortical column and whole-brain imaging with molecular contrast and nanoscale resolution. *Science* **363**, eaau8302 (2019).

119. Dean, K. M., Roudot, P., Welf, E. S., Danuser, G. & Fiolka, R. Deconvolution-free subcellular imaging with axially swept light sheet microscopy. *Biophys. J.* **108**, 2807–2815 (2015).

120. Pende, M. et al. High-resolution ultramicroscopy of the developing and adult nervous system in optically cleared Drosophila melanogaster. *Nat. Commun.* **9**, 4731 (2018).

121. Amat, F. et al. Efficient processing and analysis of large-scale light-sheet microscopy data. *Nat. Protoc.* **10**, 1679–1696 (2015).

122. Pietzsch, T., Saalfeld, S., Preibisch, S. & Tomancak, P. BigDataViewer: visualization and processing for large image data sets. *Nat. Methods* **12**, 481–483 (2015).
This article describes BigDataViewer, which provides a well-engineered software framework to navigate and compute on arbitrarily large image data sets that is integrated into the popular Fiji ecosystem.

123. Schindelin, J., Rueden, C. T., Hiner, M. C. & Eliceiri, K. W. The ImageJ ecosystem: an open platform for biomedical image analysis. *Mol. Reprod. Dev.* **82**, 518–529 (2015).

124. Pietzsch, T., Preibisch, S., Tomančák, P. & Saalfeld, S. ImgLib2—generic image processing in Java. *Bioinformatics* **28**, 3009–3011 (2012).

125. Preibisch, S., Saalfeld, S., Schindelin, J. & Tomancak, P. Software for bead-based registration of selective plane illumination microscopy data. *Nat. Methods* **7**, 418–419 (2010).

126. Preibisch, S. et al. Efficient Bayesian-based multiview deconvolution. *Nat. Methods* **11**, 645–648 (2014).

127. Balazs, B., Deschamps, J., Albert, M., Ries, J. & Hufnagel, L. A real-time compression library for microscopy images. Preprint at *bioRxiv* https://doi.org/10.1101/164624 (2017).

128. Cheeseman, B. L., Günther, U., Susik, M., Gonciarz, K. & Sbalzarini, I. F. Forget pixels: adaptive particle representation of fluorescence microscopy images. *Nat. Commun.* **9**, 5160 (2018).

129. Schindelin, J. et al. Fiji: an open-source platform for biological-image analysis. *Nat. Methods* **9**, 676–682 (2012).

130. Tomer, R., Denes, A. S., Tessmar-Raible, K. & Arendt, D. Profiling by image registration reveals common origin of annelid mushroom bodies and vertebrate pallium. *Cell* **142**, 800–809 (2010).

131. Heckscher, E. S. et al. Atlas-builder software and the eNeuro atlas: resources for developmental biology and neuroscience. *Development* **141**, 2524–2532 (2014).

132. Ronneberger, O. et al. ViBE-Z: a framework for 3D virtual colocalization analysis in zebrafish larval brains. *Nat. Methods* **9**, 735–742 (2012).

133. Bogovic, J. A., Hanslovsky, P., Wong, A. & Saalfeld, S. in *2016 IEEE 13th International Symposium on Biomedical Imaging (ISBI)* 1123–1126 (IEEE, 2016).

134. Zheng, Z. et al. A complete electron microscopy volume of the brain of adult Drosophila melanogaster. *Cell* **174**, 730–743.e22 (2017).

135. Sommer, C. S., Kothe C., Hamprecht U. & Ilastik F. A. in *2011 IEEE International Symposium on Biomedical Imaging: From Nano to Macro* 230–233 (IEEE, 2011).

136. Fürth, D. et al. An interactive framework for whole-brain maps at cellular resolution. *Nat. Neurosci.* **21**, 139–149 (2018).

137. Oh, S. W. et al. A mesoscale connectome of the mouse brain. *Nature* **508**, 207–214 (2014).

138. Lein, E. S. et al. Genome-wide atlas of gene expression in the adult mouse brain. *Nature* **445**, 168–176 (2007).

139. Saalfeld, S., Cardona, A., Hartenstein, V. & Tomancak, P. CATMAID: collaborative annotation toolkit for massive amounts of image data. *Bioinformatics* **25**, 1984–1986 (2009).

140. Schneider-Mizell, C. M. et al. Quantitative neuroanatomy for connectomics in Drosophila. *eLife* **5**, e12059 (2016).
This article describes the first applications of crowdsourcing of connectome tracing through the Web-based CATMAID framework.

141. Amat, F. et al. Fast, accurate reconstruction of cell lineages from large-scale fluorescence microscopy data. *Nat. Methods* **11**, 951–958 (2014).

142. Bria, A. & Iannello, G. TeraStitcher - a tool for fast automatic 3D-stitching of teravoxel-sized microscopy images. *BMC Bioinforma.* **13**, 316 (2012).

143. Wolff, C. et al. Multi-view light-sheet imaging and tracking with the MaMuT software reveals the cell lineage of a direct developing arthropod limb. *eLife* **7**, e34410 (2018).

144. Moffitt, J. R. et al. Molecular, spatial, and functional single-cell profiling of the hypothalamic preoptic region. *Science* **362**, eaau5324 (2018).

145. Bakutkin, V. V., Maksimova, I. L., Semyonova, T. N., Tuchin, V. V. & Kon, I. L. in *Ophthalmic Technologies V* 137–142 (SPIE, 1995).

146. Zimnyakov, D. A., Tuchin, V. V., Michin, A. A., Kon, I. L. & Serov, A. N. in *Ophthalmic Technologies VI* 233–243 (SPIE, 1996).

147. Tuchin, V. V. et al. in *Photon Propagation in Tissues II* 118–143 (SPIE, 1996).

148. Tuchin, V. V. et al. Light propagation in tissues with controlled optical properties. *J. Biomed. Opt.* **2**, 401–417 (1997).

149. Bashkatov, A. N. et al. in *Ophthalmic Technologies IX* 311–320 (SPIE, 1999).

150. Tuchin, V. V. et al. Optics of living tissues with controlled scattering properties. *Proc. SPIE* **3863**, 10–21 (1999).

151. Tuchin, V. V., Xu, X. & Wang, R. K. Dynamic optical coherence tomography in studies of optical clearing, sedimentation, and aggregation of immersed blood. *Appl. Opt.* **41**, 258–271 (2002).

152. Xu, X., Wang, R. K., Elder, J. B. & Tuchin, V. V. Effect of dextran-induced changes in refractive index and aggregation on optical properties of whole blood. *Phys. Med. Biol.* **48**, 1205–1221 (2003).

153. Liu, H., Beauvoit, B., Kimura, M. & Chance, B. Dependence of tissue optical properties on solute-induced changes in refractive index and osmolarity. *J. Biomed. Opt.* **1**, 200–211 (1996).

154. Vargas, O., Chan, E. K., Barton, J. K., Rylander, H. G. & Welch, A. J. Use of an agent to reduce scattering in skin. *Lasers Surg. Med.* **24**, 133–141 (1999).

155. Vargas, G., Chan, K. F., Thomsen, S. L. & Welch, A. J. Use of osmotically active agents to alter optical properties of tissue: effects on the detected fluorescence signal measured through skin. *Lasers Surg. Med.* **29**, 213–220 (2001).

156. Wang, R. K., Xu, X., Tuchin, V. V. & Elder, J. B. Concurrent enhancement of imaging depth and contrast for optical coherence tomography by hyperosmotic agents. *JOSA B* **18**, 948–953 (2001).

157. Xu, X. & Wang, R. K. The role of water desorption on optical clearing of biotissue: studied with near infrared reflectance spectroscopy. *Med. Phys.* **30**, 1246–1253 (2003).

158. Jiang, J. & Wang, R. K. Comparing the synergistic effects of oleic acid and dimethyl sulfoxide as vehicles for optical clearing of skin tissue in vitro. *Phys. Med. Biol.* **49**, 5283–5294 (2004).

159. Choi, B. et al. Determination of chemical agent optical clearing potential using in vitro human skin. *Lasers Surg. Med.* **36**, 72–75 (2005).

160. Staudt, T., Lang, M. C., Medda, R., Engelhardt, J. & Hell, S. W. 2,2′-Thiodiethanol: a new water soluble mounting medium for high resolution optical microscopy. *Microsc. Res. Tech.* **70**, 1–9 (2007).

161. Aoyagi, Y., Kawakami, R., Osanai, H., Hibi, T. & Nemoto, T. A rapid optical clearing protocol using 2,2′-thiodiethanol for microscopic observation of fixed mouse brain. *PLOS ONE* **10**, e0116280 (2015).

162. Kuwajima, T. et al. ClearT: a detergent- and solvent-free clearing method for neuronal and non-neuronal tissue. *Development* **140**, 1364–1368 (2013).

163. Tsai, P. S. et al. Correlations of neuronal and microvascular densities in murine cortex revealed by direct counting and colocalization of nuclei and vessels. *J. Neurosci.* **29**, 14553–14570 (2009).

164. Hou, B. et al. Scalable and DiI-compatible optical clearance of the mammalian brain. *Front Neuroanat.* **9**, 19 (2015).

165. Diogo, R., Siomava, N. & Gitton, Y. Development of human limb muscles based on whole-mount immunostaining and the links between ontogeny and evolution. *Development* **146**, dev180349 (2019).

166. LaVision BioTec. The UltraMicroscope setup. *LaVision BioTec* https://www.lavisionbiotec.com/products/UltraMicroscope/specification.html (2019).

167. Zeiss. Lightsheet Z1. *Zeiss* https://www.zeiss.com/microscopy/us/products/imaging-systems/lightsheet-z-1.html#downloads (2019).

168. Engelbrecht, C. J. & Stelzer, E. H. Resolution enhancement in a light-sheet-based microscope (SPIM). *Opt. Lett.* **31**, 1477–1479 (2006).

169. Schwarz, M. K. et al. Fluorescent-protein stabilization and high-resolution imaging of cleared, intact mouse brains. *PLOS ONE* **10**, e0124650 (2015).

170. Jing, D. et al. Tissue clearing of both hard and soft tissue organs with the PEGASOS method. *Cell Res.* **28**, 803–818 (2018).

171. Becker, K., Jährling, N., Saghafi, S., Weiler, R. & Dodt, H. U. Chemical clearing and dehydration of GFP expressing mouse brains. *PLOS ONE* **7**, e33916 (2012).
172. Scott, G. D., Blum, E. D., Fryer, A. D. & Jacoby, D. B. Tissue optical clearing, three-dimensional imaging, and computer morphometry in whole mouse lungs and human airways. *Am. J. Respir. Cell. Mol. Biol.* **51**, 43–55 (2014).
173. Ertürk, A., Lafkas, D. & Chalouni, C. Imaging cleared intact biological systems at a cellular level by 3DISCO. *J. Vis. Exp.* https://doi.org/10.3791/5138 (2014).
174. Epp, J. R. et al. Optimization of CLARITY for clearing whole-brain and other intact organs. *eNeuro* **2**, ENEURO.0022-15.2015 (2015).
175. Abe, T. et al. Visualization of cell cycle in mouse embryos with Fucci2 reporter directed by Rosa26 promoter. *Development* **140**, 237–246 (2013).
176. Breuss, M. et al. The expression of tubb2b undergoes a developmental transition in murine cortical neurons. *J. Comp. Neurol.* **523**, 2161–2186 (2015).
177. Sekitani, T. et al. Ultraflexible organic amplifier with biocompatible gel electrodes. *Nat. Commun.* **7**, 11425 (2016).
178. Mizutani, H. et al. Transparency-enhancing technology allows three-dimensional assessment of gastrointestinal mucosa: a porcine model. *Pathol. Int.* **68**, 102–108 (2018).
179. Warner, C. A. et al. An optical clearing technique for plant tissues allowing deep imaging and compatible with fluorescence microscopy. *Plant. Physiol.* **166**, 1684–1687 (2014).
180. Hasegawa, J. et al. Three-dimensional imaging of plant organs using a simple and rapid transparency technique. *Plant Cell Physiol.* **57**, 462–472 (2016).
181. Chen, L. et al. UbasM: an effective balanced optical clearing method for intact biomedical imaging. *Sci. Rep.* **7**, 12218 (2017).
182. Kurihara, D., Mizuta, Y., Sato, Y. & Higashiyama, T. ClearSee: a rapid optical clearing reagent for whole-plant fluorescence imaging. *Development* **142**, 4168–4179 (2015).
183. Wang, Z. et al. Imaging transparent intact cardiac tissue with single-cell resolution. *Biomed. Opt. Express* **9**, 423–436 (2018).
184. Yu, T. et al. RTF: a rapid and versatile tissue optical clearing method. *Sci. Rep.* **8**, 1964 (2018).
185. Li, W., Germain, R. N. & Gerner, M. Y. Multiplex, quantitative cellular analysis in large tissue volumes with clearing-enhanced 3D microscopy (C$_e$3D). *Proc. Natl Acad. Sci. USA* **114**, E7321–E7330 (2017).
186. Lai, H. M. et al. Rationalisation and validation of an acrylamide-free procedure in three-dimensional histological imaging. *PLOS ONE* **11**, e0158628 (2016).
187. Xu, N. et al. Fast free-of-acrylamide clearing tissue (FACT)—an optimized new protocol for rapid, high-resolution imaging of three-dimensional brain tissue. *Sci. Rep.* **7**, 9895 (2017).
188. Perbellini, F. et al. Free-of-Acrylamide SDS-based tissue clearing (FASTClear) for three dimensional visualization of myocardial tissue. *Sci. Rep.* **7**, 5188 (2017).

Author contributions
H.R.U., A.E., K.C., V.G., A.C. and P.J.K. researched data for the article. All the authors contributed to substantial discussion of its content, wrote the article and reviewed and edited the manuscript before submission.

Competing interests
H.R.U. is a co-inventor on a patent applications covering the CUBIC reagents (PCT/JP2014/070618 (pending), patent applicant is RIKEN, other co-inventors are E. A. Susaki and K. Tainaka; PCT/JP2017/016410 (pending), patent applicant is RIKEN, other co-inventors are K. Tainaka and T. Murakami) and a co-founder of CUBICStars Inc. A.E. is the applicant and the inventor on a patent application for technologies relating to vDISCO clearing (PCT/EP2018/063098 (pending)). K.C. is the inventor or a co-inventor on patents and patent appli-cations for CLARITY (PCT/US2013/031066 (active), patent applicant is Stanford University, co-inventor is K. A. Deisseroth), stochastic electrotransport (PCT/US2015/024297 (active), patent applicant is MIT), SHIELD (PCT/US2016/064538 (pending), applicant is Massachusetts Institute of Technology (MIT), other co-inventors are E. Murray and J. H. Cho), SWITCH (PCT/US2016/064538 (pending), applicant is MIT, other co-inventors are E. Murray and J. H. Cho) and MAP (PCT/US2017/030285 (pending), applicant is MIT, other co-inventors are T. Ku, J. M. Swaney and J. Y. Park) and a co-founder of LifeCanvas Technologies. V.G. is a co-inventor on patent applications covering PACT and PARS (PCT/US2014/048985 (active), applicant is California Institute of Technology, other co-inventors are V. Gradinaru and B. Yang) and adeno-associated virus (US14/485,024 (active), applicant is California Institute of Technology, other co-inventors are B. E. Deverman, P. H. Patterson and V. Gradinaru) technologies. P.J.K. is an inventor or co-inventor on patents and patent applications covering multiview imag-ing (US14/049,470 (active), applicant is Howard Hughes Medical Institute) and adaptive light-sheet microscopy (PCT/US2017/038970 (pending), applicant is Howard Hughes Medical Institute, other co-inventors are R. K. Chhetri and L. A. Royer). P.T. and A.C. declare no competing interests.

Peer review information
Nature Reviews Neuroscience thanks S. Gentleman and the other, anonymous, reviewer(s) for their contribution to the peer review of this work.

Publisher's note
Springer Nature remains neutral with regard to jurisdictional claims in published maps and institutional affiliations.

Supplementary information
Supplementary information is available for this paper at https://doi.org/10.1038/s41583-019-0250-1.